2-9-2010

A prototype Compton imager : simulations, measurements and algorithm development

Shawn Tornga

Follow this and additional works at: https://digitalrepository.unm.edu/ne_etds

Recommended Citation
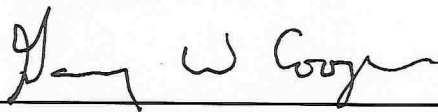
Shawn R. Tornga
_____
Candidate

Nuclear Engineering
_____
Department

This thesis is approved, and it is acceptable in quality
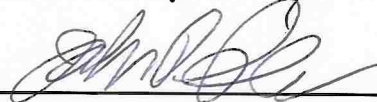and form for publication:

Approved by the Thesis Committee:

_____ ,Chairperson

Adam Hecht   _____

John P. Sullivan   _____

_____

_____

_____

_____

_____

i

A Prototype Compton Imager - Simulations, Measurements and
Algorithm Development

by

Shawn R. Tornga

Bachelor of Science, Physics, Michigan State University, 2005

THESIS

Submitted in Partial Fulfillment of the
Requirements for the Degree of

Master of Science
Nuclear Engineering

The University of New Mexico
Albuquerque, New Mexico

December, 2009

For Stephanie

ACKNOWLEDGEMENTS

I heartily acknowledge Dr. Gary Cooper, my academic advisor and thesis chair, for continuing to encourage me through the years of classroom teachings and the long number of months writing these chapters. His guidance and professional style will remain with me as I continue my career. I would like to thank Dr. Adam Hecht for his guidance and participation during my defense of this thesis.

I would also like to thank my research mentors, Dr. John P. Sullivan, Dr. Mohini Rawool-Sullivan, and Dr. Mark Wallace, for their valuable recommendations pertaining to this study and assistance in my professional development. Gratitude is extended to the Department of Energy for the funding to pursue this research.

To my parents, Kurt and Denise, and my brother Corey, who gave to immeasurable support over the years. Your encouragement is greatly appreciated. And finally to my wife, Stephanie, your love and support have made this possible.

A Prototype Compton Imager - Simulations, Measurements
and Algorithm Development

by

Shawn R. Tornga

ABSTRACT OF THESIS

Submitted in Partial Fulfillment of the
Requirements for the Degree of

Master of Science
Nuclear Engineering

The University of New Mexico
Albuquerque, New Mexico

December, 2009

A PROTOTYPE COMPTON IMAGER - SIMULATIONS, MEASUREMENTS AND ALGORITHM DEVELOPMENT

By

Shawn R. Tornga

B.S., Physics, Michigan State University, 2005

M.S., Nuclear Engineering, University of New Mexico, 2009

ABSTRACT

Compton imaging is a gamma ray imaging technique that has possible applications in the nuclear and medical industries. Compton imaging can localize the origin of a scattered gamma ray, to a cone, using a minimum of two position and energy measurements. The projection of many cones will overlap at a common point leading to the actual source position. A prototype Compton imager (PCI) has been constructed at Los Alamos National Laboratory (LANL) that uses a combination of silicon and CsI detectors. A model of the PCI has been simulated and validated, showing good agreement with measured data. The angular resolution of the PCI was measured to be 0.156 radians FWHM. Additionally, a method for determining the source-to-detector distance in the near field has been developed and demonstrated. The algorithm presented has the ability to determine the source-to-detector distance in the near field within 1 cm of the actual distance.

While traditional back-projection algorithms are adequate for imaging of single point-like sources they are not sufficient to resolve extended shapes or closely spaced

multiple point-like sources. Iterative algorithms may provide the necessary deconvolution. Maximum Likelihood Expectation Maximization (MLEM) is an iterative statistical algorithm that reconstructs the most probable source distribution for a given data set. Normally, MLEM makes computations for each possible combination of energy and position, however this becomes a prohibitively large problem for both analysis time and hardware memory limits, depending on the data set. List Mode MLEM attempts to circumvent the calculation of every combination of energy and position and relies on the probability of the given data being observed. An algorithm using List-Mode MLEM is of interest because the number of calculations required for reconstruction is substantially less than that of other iterative processes but will enable imaging of both point and extended sources. This type of algorithm has been written and successfully applied to both experimental data from the PCI and simulations of the PCI. The algorithm will be demonstrated to improve detection of both point-like and extended sources.

Contents

List of Figures

List of Tables

Chapter 1

INTRODUCTION

Gamma-ray imaging is widely used as a research tool in nuclear medicine and astrophysics. Additionally, research in the use of gamma-ray imaging for waste monitoring and nuclear nonproliferation began in the 1990s. Since then efforts to develop better detection technologies has gained increased attention. In particular, imaging technologies which allow passive gamma-ray detectors to localize sources and reject backgrounds from irrelevant directions and sources are being sought. This capability would provide the improved sensitivity needed for sensing nuclear materials from distances of tens of meters and beyond. Compton imaging was recognized as one such imaging technique. It is based on the Compton scattering interaction (scattering of a gamma ray from an electron). Compton scattering preserves information about the direction and energy of incident gamma rays if the scattering by-products can be precisely measured. Various Compton imaging designs have been studied for use in many fields including counterterrorism. One such effort was carried out by the Naval Research Laboratory along with the University of California at Berkeley based on their astrophysics expertise. This effort focused on the development of Compton imagers that used thick, position sensitive, solid-state detectors [1]. Efforts by Lawrence

Livermore National Laboratory (along with collaborators) included development of the spectroscopic imager for gamma rays, SPEIR [2], Compton imaging with position sensitive silicon and germanium detectors [3], and coaxial germanium detectors [4]. There are many situations applicable to homeland security where it is necessary to localize the position and shape of an unknown source within a closed volume. One such application is cargo screening, where it is inefficient and costly to open containers to search for nuclear material. Other applications include screening the contents of suspicious objects while maintaining a safe distance and passive searching of public areas where nuclear material may be present.

1.1 Why Compton Imaging?

While Compton imaging is not a new technique, recent advances in material fabrication and signal processing capabilities make building a Compton imaging device more efficient. Compton imaging is also one choice for a gamma-ray imaging system capable of performing three-dimensional imaging and provides the means to image gamma rays without the use of a collimator. Eliminating heavy collimators has the advantage of reducing the overall weight of the system, which is an important factor when considering a fieldable device, especially in airborne and space applications. Compton imaging also increases the field-of-view (FOV) from the small fraction of 4π for collimated detectors, up to full 360° imaging. There are some drawbacks however, including the medium to high cost.

While most of these factors demonstrate the attractiveness of a Compton imager, much of the capability of any imaging system hinges on the quality of the algorithms used to reconstruct data. The goal of this thesis is to present an existing prototype

Compton imager designed and built at Los Alamos National Laboratory (LANL). Monte Carlo [5, 6] simulations will be performed and validated against measured data. If the simulations can accurately model the true response of the laboratory detector, larger detectors can be designed and modeled confidently to optimize efficiency and cost before construction. In addition algorithms developed to maximize the information content obtained from the imager will be developed and presented. Image reconstruction algorithms will include both geometric back-projection and maximum likelihood methods. Beyond image reconstruction, a method for determining the source-to-detector distance is needed when imaging sources at unknown positions. A method for determining the source-to-detector distance was developed in this work and will be presented.

1.2   Prior Work

Compton imaging has been of interest to researchers in both the medial imaging and astrophysics communities since the early 1980's. More recently, the potential value of Compton imaging for homeland security applications has been recognized. Currently there are several efforts underway examining how new detector technologies can be applied to Compton imaging as well as utilizing advanced algorithms to improve the detection capabilities of current systems.

Wulf *et al.* [8] at the Naval Research Laboratory (NRL) report the application of germanium strip detectors for the construction of a Compton telescope. As the gamma ray's energy increases, more material is required to stop it. If detectors with good position and energy resolution are thick enough to have multiple Compton scatters then the gamma does not need to be fully absorbed. Thicker detectors require

depth resolution or a large separation between detectors to accurately determine the scattering angle. Unfortunately, a large separation between detectors reduces the efficiency of the instrument. Wulf proposed a detector system capable of both stopping low energy gamma rays completely and using multiple Compton scatters for high-energy gamma rays, however this requires expensive electronics and complex event reconstruction algorithms.

Similarly, Vetter *et al.* [9] at Lawrence Livermore National Laboratory (LLNL) have developed an imaging system using position-sensitive high-purity germanium (HPGe) and lithium drifted silicon detectors (Si(Li)) [10]. This system should allow for imaging of gamma ray sources with higher sensitivity than collimator based systems with the use of advanced 3D gamma ray tracking techniques. They have implemented a Compton camera built of a single double-sided strip HPGe detector with a strip pitch of 2 mm. They report three dimensional position resolution of 0.5 mm at 122 keV using simple pulse shape analysis techniques. Not only did they construct the detector system but they implemented maximum likelihood reconstruction procedures to optimize image quality with potential applications outside of Compton imaging. This technique will be discussed in section 6.2 of this thesis.

For space applications, Tanaka *et al.* [11] at the Institute of Space and Astronautical Science (JAXA) have developed a Si/CdTe semiconductor Compton telescope. This effort was aimed at developing a Compton telescope based on high resolution silicon and CdTe imaging devices in order to obtain a high sensitivity astrophysical observation in the sub-MeV gamma-ray region. The Compton telescope consists of a double-sided silicon strip detector (DSSD) surrounded by CdTe pixel detectors. Similar to the LANL prototype Compton imager [12], Tanaka uses silicon as a scattering

detector but uses CdTe as absorbing detectors rather than CsI.

In 2004 Xu *et al.* of the University of Michigan proposed a unique method of Compton imaging [13]. In their method, the use of a single CdZnTe (CZT) semiconductor detector with 3D position resolution, as well as energy information of each interaction, is used to perform Compton imaging. The detector used is a single 15 x 15 x 10 mm crystal of CZT. Since any point in the detector can be the scatter position, it allows them to do 4π imaging in the near-field. This is a novel approach because it is the first semiconductor based 4π Compton imaging system. They also worked to improve on the algorithms used in Compton imaging, attempting to reconstruct images using filtered back-projection and maximum likelihood techniques.

Aprile from Columbia University and collaborators developed a Compton telescope for space applications called LXeGRIT [14]. LXeGRIT was the first Compton telescope to perform complete 3D reconstruction of the sequence of interactions of individual gamma rays in a single, position-sensitive, liquid xenon time projection chamber for space applications. Characterization of LXeGRIT included both laboratory and balloon flight missions.

Each of the examples of Compton imaging given have drawbacks associated. The use of HPGe detectors is costly due to cooling constraints. CZT is still a relatively new and expensive material that is not available in large quantities. Also, commercially available CZT rarely operates as expected. In addition, the angular uncertainty associated with measurements taken from the currently available small CZT crystal sizes can be large. Silicon is an excellent room temperature detector but is inefficient at stopping high-energy gamma rays. All of these factors come into play when designing a Compton imager. The LANL prototype Compton imager (PCI) is a com-

bination of some of the elements presented here with a focus on improved angular resolution, simulations and advanced algorithm development. This thesis will focus on the operation and performance characteristics of the PCI as well as algorithm development. However, before an imaging system can be constructed there must be an understanding of the physical interaction processes occurring in the detector.

1.3   Interaction Processes

Understanding the relevant interaction processes is a necessary step towards being able to reconstruct Compton camera data. The three major interactions relevant to Compton cameras are photoelectric absorption, Compton scattering and pair production. Each of the three processes has an interaction probability which depends on photon energy and the material. Figure 1.1 plots the attenuation values (cm^2/g) for both CsI (left) and silicon (right) [15]. It can be seen that Compton scattering is the dominant gamma ray interaction process in silicon between 0.1 and 10 MeV and that photoelectric absorption is the dominant process in CsI below about 0.3 MeV.

1.3.1   Photoelectric Absorption

Photoelectric absorption is a process in which photons interact with bound electrons in an absorber atom, usually tightly bound K shell electrons. Following absorption, the incident photon produces a photoelectron. The photoelectron emerges with energy E_e, as described by equation 1.1, where E_γ is the gamma ray energy and E_b is the binding energy of the photoelectron, or the energy required to remove it from its shell [16]. Photoelectric absorption is the dominant interaction mechanism for low-energy gamma rays.
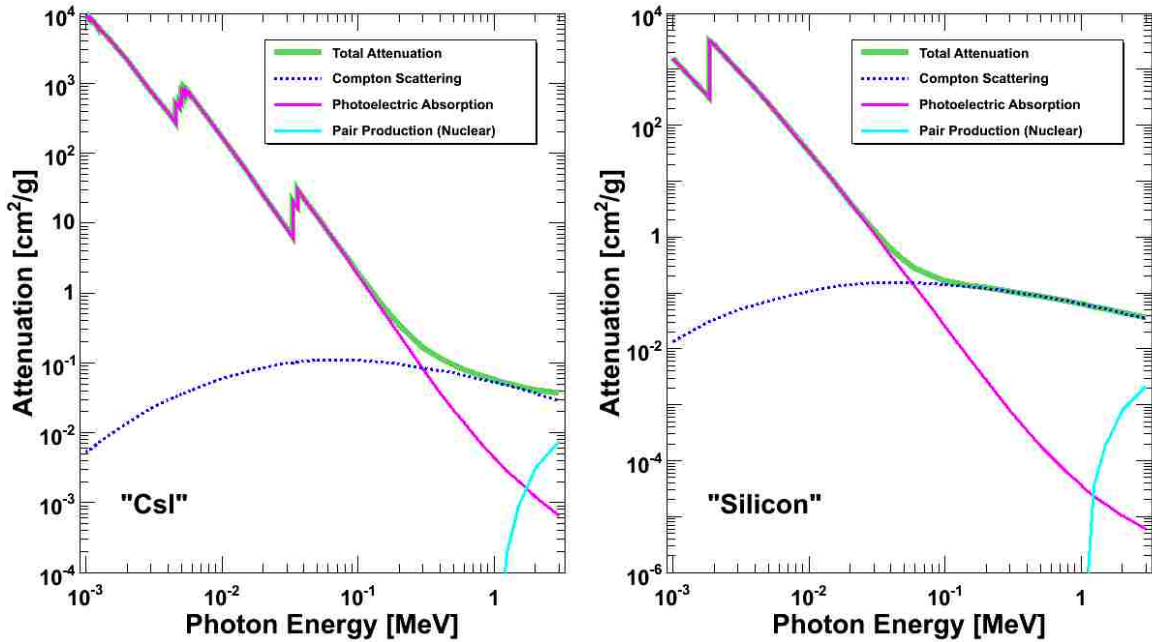
Figure 1.1: Photon attenuation values for CsI (left) and silicon (right).

$$E_e = E_\gamma - E_b \tag{1.1}$$

1.3.2 Compton Scattering

Compton, or incoherent scattering, was first explained by Arthur Compton in 1923 [17]. It was a significant discovery and earned him the Nobel prize in Physics. A key reason for giving him the Nobel prize was his recognition of the fact that a photon could behave like a particle in some circumstances. Compton scattering is an interaction process by which there is a decrease in energy, or increase in wavelength, of an incident photon when it elastically scatters off an electron in matter. The interaction between the photon and an electron in the scattering material results in a portion of the initial photon energy being imparted to the electron, causing it to recoil and

the photon continuing on in a direction different from the original direction. Figure 1.2 shows a schematic of the Compton interaction where E_γ is the incident photon energy, E_γ' is the scattered photon energy, E_e' is the energy of the recoil electron, θ_γ is the photon scattering angle and ϕ_e is the recoil electron scattering angle.
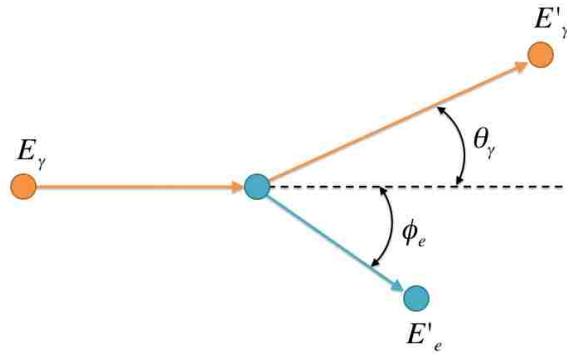
Figure 1.2: The Compton scattering interaction.

The change in direction of the photon is proportional to the energy imparted to the electron and can be calculated. Compton scattering is the dominant interaction mechanism for medium energy photons (0.5 to 3.5 MeV) in most materials. The kinematics of Compton scattering can be derived using conservation of energy (1.2) and momentum. Although the target electron does have non-zero initial momentum, its initial momentum is not known. As a result, the initial total energy of the electron is assumed to be its rest energy (0.511 MeV) and its momentum 0. Taking these assumptions into account, conservation of momentum can be expressed in the form of (1.3).

$$E_\gamma + E_e = E_\gamma' + E_e' \tag{1.2}$$

8

$$\vec{P}_\gamma = \vec{P}'_\gamma + \vec{P}'_e \tag{1.3}$$

Solving equations 1.2 and 1.3 the relationship between photon energy and scattering angle can be obtained and is known as the Compton scattering equation [17], where m_e is the rest mass energy of an electron and c is the speed of light. The Compton scattering formula is shown in Eq. 1.4.

$$\cos\theta_\gamma = 1 + \frac{m_e c^2}{E'_e + E'_\gamma} - \frac{m_e c^2}{E'_\gamma} \tag{1.4}$$

1.3.3 Pair Production

Another process to be considered in a Compton camera system is pair production. Pair production is the creation of an electron and positron from a photon. This process occurs as a result of the interaction of the photon with the electromagnetic field of the nucleus of a target atom. This interaction can also take place with an electron but only at higher energies that are not of interest for Compton imaging. Pair production can only occur when the amount of energy available is greater than or equal to the rest mass energy of the pair (1.022 MeV). Figure 1.3 shows the nuclear pair production interaction where θ is the polar angle of both the exiting position and electron.

1.3.4 Doppler Broadening

Doppler broadening is an effect brought on by the electrons involved in the Compton scatter interaction. Equation 1.4 is based on the assumption that the electrons are initially free or unbound. The electrons, however, are neither free nor at rest, but in motion and bound to a nucleus [19]. This has several effects on the kinematics of
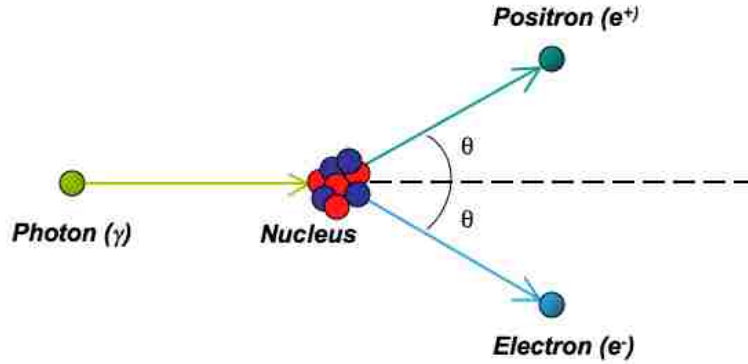
Figure 1.3: The nuclear pair production interaction.

the Compton scatter. First, the total scattering probability changes as defined by the Klein-Nishina scattering cross-section [20]. Second, the scattering angle distribution changes, and finally the energy distribution between the electron and the gamma ray changes. All of these consequences give rise to a fundamental, lower limit for the angular resolution of a Compton camera. It is safe to assume that in the case of the PCI (and any other detector) this effect is uncorrectable. In the case of the PCI however, the effect is generally masked by the finite energy resolution of the silicon and CsI detectors and the size of the CsI(Tl) elements. Also, the effect is most pronounced at low-energy (<150 keV).

Since the effects of Doppler broadening are inherent to a material, as the atomic number (Z) of a material increases, the effects of Doppler broadening increase. The choice of silicon as a scattering detector in the PCI was made because silicon minimizes the contribution of Doppler broadening to the angular resolution while maintaining the reasonable energy resolution expected from a room temperature semiconductor [7].

Chapter 2

THE LANL PROTOTYPE COMPTON IMAGER

The LANL built prototype Compton imager (PCI) consists of three silicon scattering detectors and a backplane of CsI absorbing detectors, separated by an adjustable distance. Incident gamma rays are expected to Compton scatter in the thin silicon detectors and photo-absorb in the CsI array. Figure 2.1 shows a drawing of the complete PCI. The silicon planes are housed in light-tight, plastic bellows because of their high sensitivity to light. This chapter will describe both the silicon and CsI detector elements as well as readout electronics. Additionally, signal processing, triggering and data acquisition will be discussed.

2.1   Silicon Scattering Detectors

The silicon planes were fabricated at Brookhaven National Laboratory. Silicon was chosen as the scattering detector material because its properties as a radiation detector are well known and it is suitable for use at room temperature. Also, it has reasonably good energy resolution and is a low Z material which minimizes Doppler broadening [18]. Each of the three silicon scattering planes is mounted on an indi-
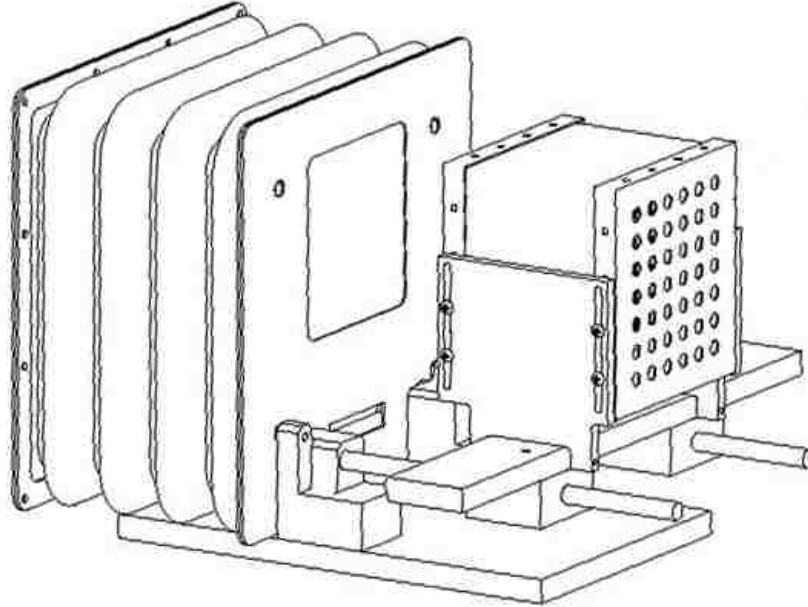
Figure 2.1: The LANL prototype Compton imager. The silicon is inside the bellows (left side) and the CsI is inside the box on the right. The holes on the CsI array are only present on the back side of the array.

vidual circuit board which contains the readout electronics and slides independently on nylon rods for easy adjustment of the spacing. Figure 2.2 shows the three silicon scattering detectors stacked together in a testbed apparatus with attached electronics.

2.1.1 Silicon Geometry

Each scattering plane is pixilated into a 16 x 20 array of 3 x 3 mm PN-type active silicon pads. The active area of each plane is approximately 48 x 60 mm. The thickness of each plane is 300 μm including a 30 μm dead layer. Figure 2.3 shows a schematic drawing of a single silicon pixel detector (not to scale).

Figure 2.2: The three silicon scattering detectors stacked together with attached electronics.

2.1.2   Silicon Electronics

The silicon front-end electronics were purchased pre-assembled, from the IDEAS corporation based on the VA-TA application specific integrated circuit (ASIC) series. Specifically the PCI uses the Va32-Rich pre-amplifier chip [21] and the Ta-32 discriminator chip [22]. Both chips are 32 channel, low power, fast triggering, ASICs, and include a fast CR-RC shaper (high and low pass filtering) followed by a level-sensitive discriminator. There are 10 ASIC chips for each silicon plane. The chips can be seen in Fig. 2.2 along the edge of the silicon. The trigger signals from each channel are multiplexed onto a single common trigger output for each chip. In addition, both chips feature a switchable, higher gain and a trim digital-to-analog converter (DAC)

13
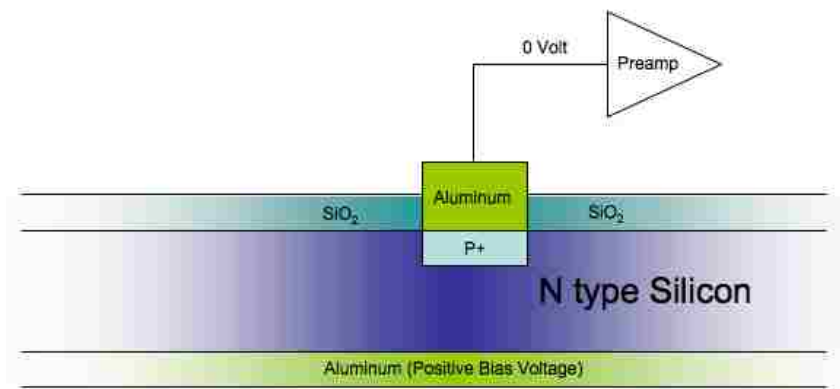
Figure 2.3: Silicon pixel detector (not to scale).

on each discriminator.

2.2 CsI Absorbing Detectors

The absorbing plane of the PCI is an array of 42 individually read-out, thallium doped, cesium iodide crystals (CsI(Tl)) with attached silicon PIN diode. Pre-amplifiers for the PIN diodes are mounted directly behind the array. The CsI(Tl)/PIN array was purchased pre-assembled from Saint Gobain and is housed in an aluminum box mounted behind the last silicon plane. CsI was chosen as the absorbing plane for the PCI because it is one of the brightest scintillator materials at 54 photons/keV and has high gamma ray stopping power due to its relatively high density (4.51 g/cm^2) and effective Z [23]. CsI is also resistant to thermal and mechanical shock [23]. Each individual crystal is read out via silicon PIN photodiode. CsI is well suited for photodiode readout because most of its emissions are in the long wavelength part of the spectrum ($\lambda > 500$ nm), which is another reason it was chosen. Photodiode readout allows the detector to operate at relatively low voltage (~ 60 V). Unfortunately CsI does exhibit

14

longer decay time ($\sim 1\ \mu$s for gamma rays) which makes it a slow scintillator, limiting the capability to perform high count-rate experiments [23].

2.2.1 CsI Geometry

The CsI(Tl) absorbing plane consists of 7 rows of 6 CsI(Tl) crystals, each 14 x 12 x 10 mm, situated parallel to the imaging plane for a total of 42 detector elements. The front face of the array is located 8 cm (adjustable) behind the last of the three silicon scattering planes. Each CsI crystal is wrapped in reflective tape and has an attached silicon PIN diode for signal pickup. Pre-amplifier modules for the CsI are mounted behind the array. The entire CsI(Tl)/PIN array is housed in an aluminum enclosure. Figure 2.4 shows the CsI array with attached preamplifiers taken from GEANT4 [5] simulations of the PCI (housing is omitted). The CsI(Tl) crystals are seen in front of the array, silicon PIN diodes are shown directly behind the crystals and are connected to the preamplifier boards.

Figure 2.4: CsI array and attached preamplifiers used in the PCI (housing is omitted).

2.2.2 CsI Electronics

Each of the 42 CsI(Tl) crystals is coupled to its own Hamamatsu S3590-01 silicon PIN photodiode [24]. This particular sensor type was chosen because it has good sensitivity matching with the light output of CsI scintillators and high quantum efficiency (85% at 540 nm). Each photodiode has an epoxy resin window and a 10 x 10 mm active area. The output of the photodiode is connected to a Hamamatsu H4083 charge amplifier [25]. The H4083 is a low-noise, compact hybrid charge amplifier specifically designed to be directly attached to the S3590 series photodiode. The gain is 22 mV/MeV.

2.3 Data Acquisition

The PCI uses a combination of on-board electronics and computer software for data acquisition. Signals are processed by the triggering system and then continue on to the data acquisition computer in blocks where they are then written to a binary file. Files written by the PCI data aquisition system are processed and imaged offline using custom LANL software. The silicon, CsI and trigger logic systems will be described in this section. Figure 2.5 shows the overall logic of the data acquisition system of the PCI.

2.3.1 Silicon Signal Processing

The outputs of the silicon pixels are split into two components. The first component which is passed through an 0.2 μs shaping amplifier is called the fast signal. After shaping the fast signal goes into a leading edge discriminator and into the field programmable gate array (FPGA) that controls the trigger for silicon data acquisition.
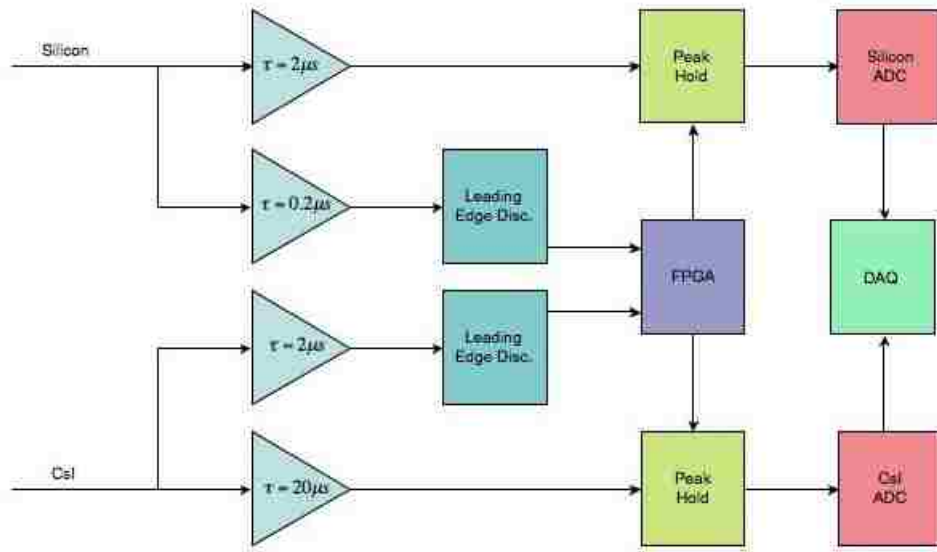
Figure 2.5: Overall logic of the data acquisition system of the PCI.

The second component of the signal is passed through a 2.0 μs shaping amplifier and is called the slow signal. After shaping the slow signal goes into a peak-hold circuit. If the amplitude of the fast signal is above the discriminator threshold, the FPGA alerts the peak-hold to capture the highest amplitude coming from the slow signal out of the shaping amplifier. After a pre-determined amount of time (long enough to ensure capture of the maximum peak amplitude) the signal is sent to an ADC. The ADC captures the signal and converts it into a value representative of energy. The ADC value is then sent to the data acquisition computer to be recorded and will later be converted into energy units in the calibration step of analysis.

2.3.2 CsI Signal Processing

The CsI readout works in much the same way as the silicon. The photodiodes output a signal to the attached charge sensitive preamplifier, which is then split into two

17

components. The first component, which is passed through a 2 μs shaping amplifier, is called the fast signal. After shaping, the fast signal goes into a leading edge discriminator followed by the FPGA that controls the trigger for CsI data acquisition. The second component is passed through a 20 μs shaping amplifier and is called the slow signal. After shaping, the slow signal goes into the peak-hold circuit. If the amplitude of the fast signal is above the discriminator threshold, the CsI peak-hold is alerted to capture the maximum amplitude of the slow signal. The peak-hold then outputs the maximum amplitude to an ADC where the amplitude is converted to an ADC value representative of energy deposited in the CsI. The ADC value is sent to the data acquisition computer to be recorded and will later be converted into energy units in the calibration step of analysis.

2.3.3 Trigger Logic

The trigger logic of the PCI is controlled by an FPGA and can be configured in many different ways. Data acquisition can be run with any of the silicon planes alone, or any combination of the three planes together. Increasing the number of silicon planes active in the trigger increases the efficiency of the detector. The CsI array can trigger the PCI alone or trigger in coincidence with a simultaneous signal in the silicon. The coincidence trigger can be set for any combination of silicon and CsI including any single silicon plane and the CsI, any two silicon planes and the CsI, or any three silicon planes and the CsI. In coincidence mode, the trigger condition is controlled by the CsI. When a CsI signal is above threshold the system waits for a silicon signal to reach threshold. Once this occurs the system then captures both the silicon and CsI signals and processes them through the ADC. Only events with at least one interaction in

both the silicon and CsI are of interest for Compton imaging. The singles triggers (no coincidence required) are used for calibration and diagnostic purposes.

2.3.4 Data Format

The data acquisition computer records events that satisfy the trigger conditions into a binary output data file. The resulting data file is separated into blocks for each recorded event sequence including the detector channel and the associated ADC value (energy deposited). The readout system operates in a 'forced' mode where all channels are written to disk for each measured event. Forced readout has the effect of adding pedestals centered at zero energy to measured data since only one channel needs to be above threshold to trigger the system. These pedestals have a finite width because of noise in the electronics and must be removed in offline analysis.

2.4 Energy Resolution

Every detector material experiences uncertainty in the measured energy versus the actual energy deposited. Additionally, signal processing can also add uncertainty to measured values known as energy resolution. The Silicon and CsI(Tl) detectors have different energy resolution. Silicon is a semiconductor material so the energy resolution is fairly stable over the energy range of interest and is assumed to be constant. CsI(Tl) is a scintillator material and the energy resolution is best described with respect to gamma-ray energy.

2.4.1 Silicon Resolution

The resolution of the silicon detectors is assumed to be constant with a sigma of approximately 5 keV, however when triggered in conjunction with the CsI array the

resolution becomes closer to 36 keV (σ). The degradation of the energy resolution results from the difference in the rise times of the silicon and CsI signals used in the trigger circuit which causes 'jitter'. The rise times are 0.2 μs for silicon and 2.0 μs for CsI. A faster scintillating material such as LaBr$_3$ [26] has been investigated as an alternative to CsI because of its fast rise time (5 ns) however has not been implemented due to budgetary constraints. Figure 2.6 shows an exaggerated look at how the difference in rise times of the silicon and CsI causes degradation of the silicon resolution.
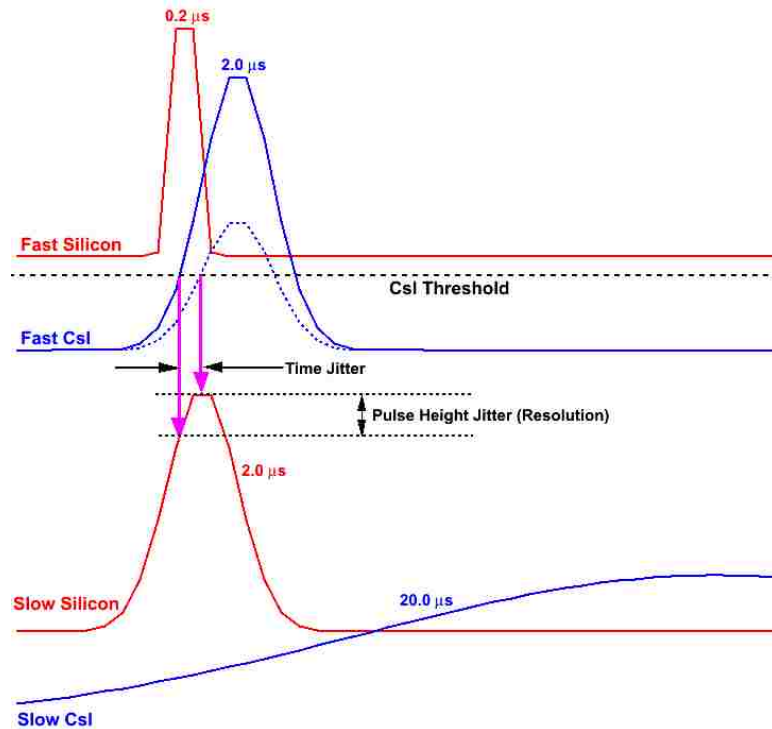
Figure 2.6: Time jitter caused by the difference in the rise times of the signals. (Not to scale).

2.4.2 CsI Resolution

Energy resolution of the CsI is energy dependent. A function that describes this dependence can be obtained experimentally by plotting the observed photopeak width as a function of energy deposited. The resolution function for the PCI was determined using ^{22}Na, ^{137}Cs and ^{54}Mn calibration sources and is given in (2.1) where E is the energy (in keV) deposited in the CsI. The function given in (2.1) is shown for energies up to 1500 keV in Fig. 2.7. The form of (2.1) comes from three factors including a constant electronic noise term (P_0^2), a statistical term related to fluxuations in photoelectron collection and conversion $(P_1 E)$ and a term related to surface effects and crystal non-uniformity $(P_2 E^2)$.

Note the low energy response of the CsI is not represented well in the fit *i.e.*, zero energy corresponds to zero uncertainty. While this is most certainly not true, the resolution function accurately describes measured data in the energy range of interest (E $>$ 350 keV). The hardware threshold on the CsI is set around 350 keV. The energy resolution of the CsI is the dominant contribution to the overall energy resolution of the PCI.

$$\sigma_{CsI} = \sqrt{P_0^2 + P_1 E + P_2 E^2} = \sqrt{(5.989 \times 10^{-5})^2 + 1.934 E + (6.190 \times 10^{-4}) E^2} \quad (2.1)$$
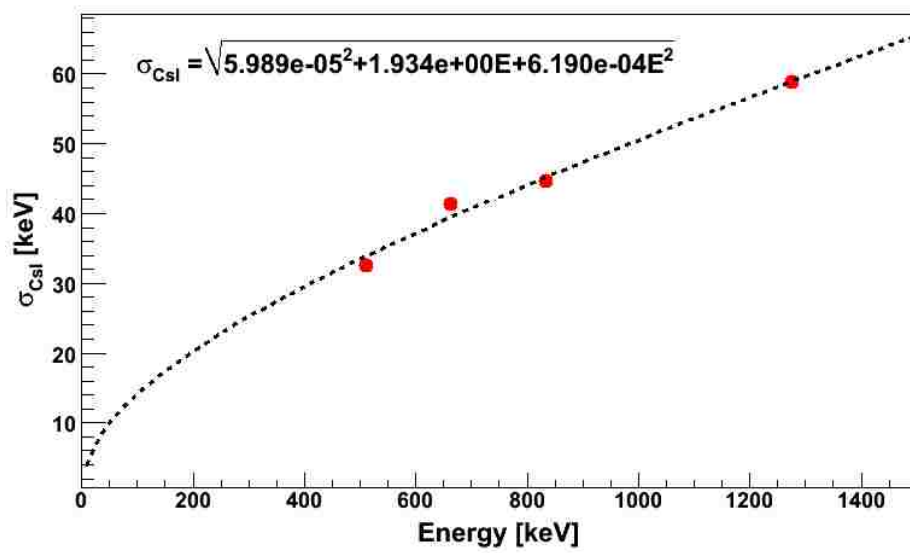
Figure 2.7: CsI energy resolution (σ) as a function of energy deposited in keV.

Chapter 3

DATA ANALYSIS

Since output data files from the PCI contain artifacts such as pedestals from the signal processing, are in terms of ADC values (not energy) and do not include calculations necessary for imaging, analysis of the data must be performed offline. Data analysis involves several steps including, subtracting the pedestal from each channel, making a correction for common-mode noise, calibrating the data, application of additional noise removal methods and parameter calculations for imaging. A suite of C/C++ programs have been developed for each of these steps. Additionally, a method for correcting the depth of interaction in the CsI detectors has been implemented.

To begin, data contained in the binary output file from the data acquisition computer (DAQ) must be unpacked into an easily accessible file format. In the case of the PCI, data are unpacked into a ROOT [27] data tree. Each entry in the tree corresponds to a single measured event sequence. For each measured sequence several variables are calculated, incuding energy deposited, number of non-zero signals (multiplicity), the x, y and z location of the maximum energy deposit, silicon total energy, CsI total energy, and the total energy deposited during the event. The specifics of each step will be detailed in this chapter.

3.1 Pedestal Subtraction

For each triggered event sequence, the signals in all 1002 detector elements of the PCI are captured and converted into a 14-bit ADC value representative of energy. The top bit gives the sign of the value and the other 13 bits give a channel between 1 and 8191. Channel 8192 is "zero" in the 14-bit number. For the majority of channels, *i.e.*, the detector elements that did not trigger the system, a zero is recorded for the event, however electronic noise gives rise to signals of non-zero amplitude. Processing of signals through the ADC that did not trigger the system results in a pedestal peak centered at zero energy. In order to ensure the integrity of the data, pedestal peaks must be removed before proceeding further with analysis. Figure 3.1 shows a sample pedestal created from reading signals from a detector element that did not trigger the system. For the pedestal shown in Fig. 3.1, zero energy corresponds to ADC channel 8268.

The number of events falling in the pedestal is larger than the number of events in any other ADC channel. Since any combination of one of the 960 silicon channels and one of the 42 CsI crystals can trigger recording of events, the majority of the signals recorded for any single channel will be zero, thus contributing to the pedestal intensity. The pedestals can be easily located since their intensity is higher than any real signal. To remove the pedestals, they must first be located.

To locate the pedestal for each detector element, the ADC channel with the largest number of events is determined. It can be seen from Fig. 3.1 that the intensity of the pedestal is much greater than any real signal. After the centroid (taken as the maximum) of each pedestal has been located, the full-width at half-maximum (FWHM) is calculated for each pedestal peak by scanning one ADC channel at a time, both

24
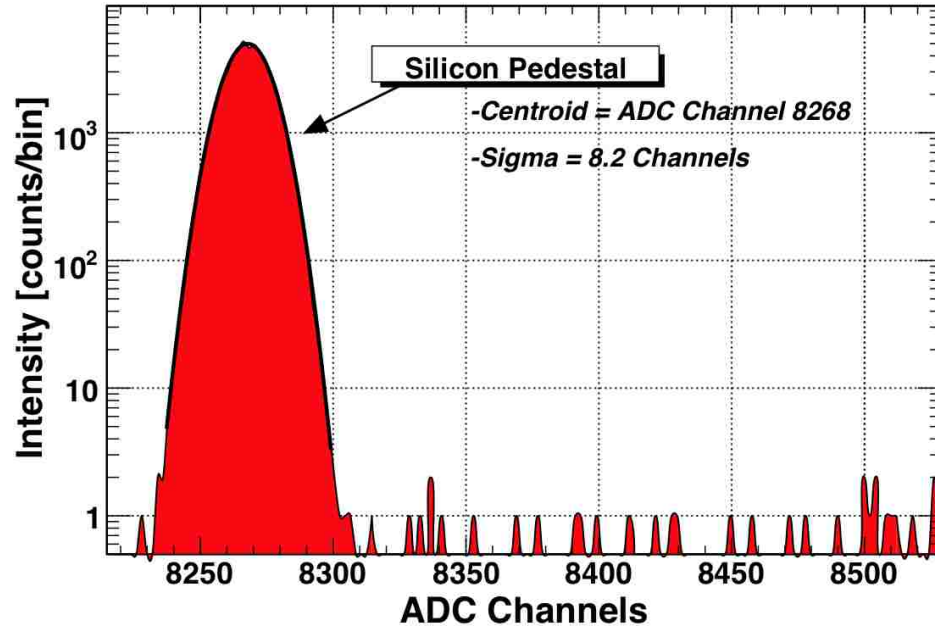
Figure 3.1: A sample pedestal created from reading zero amplitude signals from a channel that did not trigger the system.

forward and backward about the calculated maximum ADC channel (pedestal centroid) until the amplitude is less than or equal to one-half the maximum ADC channel value.

Each pedestal is then fit with a Gaussian function between plus or minus the FWHM of the pedestal centroid. The lower limit threshold is set at two FWHM above the peak for silicon and 4 FWHM above the peak for CsI. All values below that threshold are set to zero. This method assumes that each individual silicon channel has similar resolution. For some channels the resolution will differ slightly, resulting in persistent pedestal noise after subtraction or the subtraction of genuine low-energy signals. The pedestal threshold values are adjustable in the software so the user can maximize the pedestal subtraction while maintaining as many real signals

25

as possible. Figure 3.2 shows an example of a subtracted silicon pedestal where the dashed line shows the cutoff ADC channel.
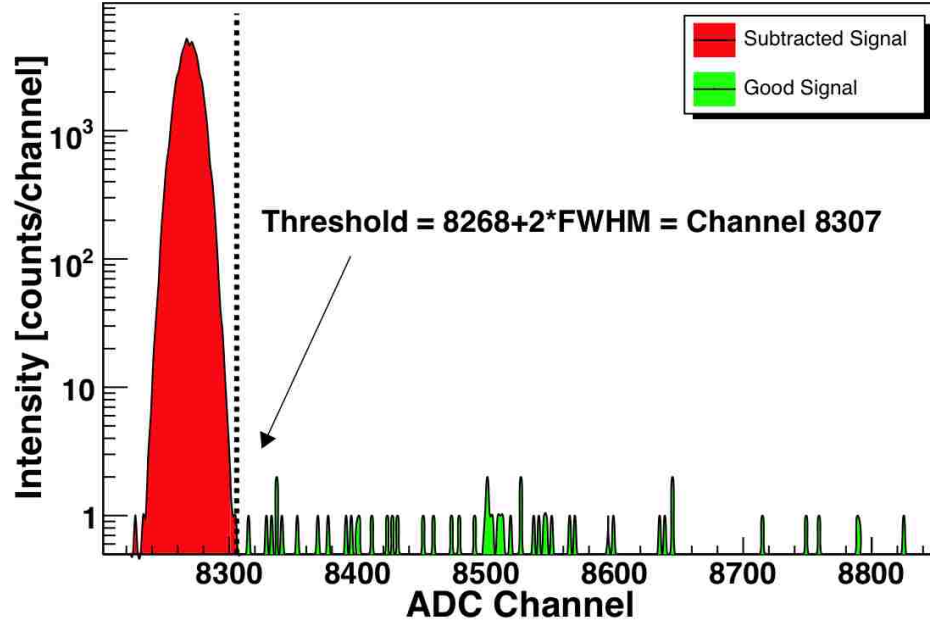
Figure 3.2: Example of silicon pedestal subtraction. The dashed line shows the point where the pedestal was cut. The events with ADC values above the pedestal represent, in most cases, "real" signals in the silicon detectors and/or noise and background.

3.2 Common-mode Noise Correction

As with most multi-channel systems, the PCI experiences some amount of common-mode noise (CMN) in both the silicon and CsI detector elements due to noise from the power supplies and other sources. This affects all input signals equally. CMN can increase the uncertainty of the recorded signal amplitude by $\pm I_{noise}/2$ where I is the maximum amplitude of the noise. Figure 3.3 sketches an example of how noise in the electronics can affect the captured input signal. Two identical input signals result in two different recorded signal amplitudes, one too low and one too high.

26
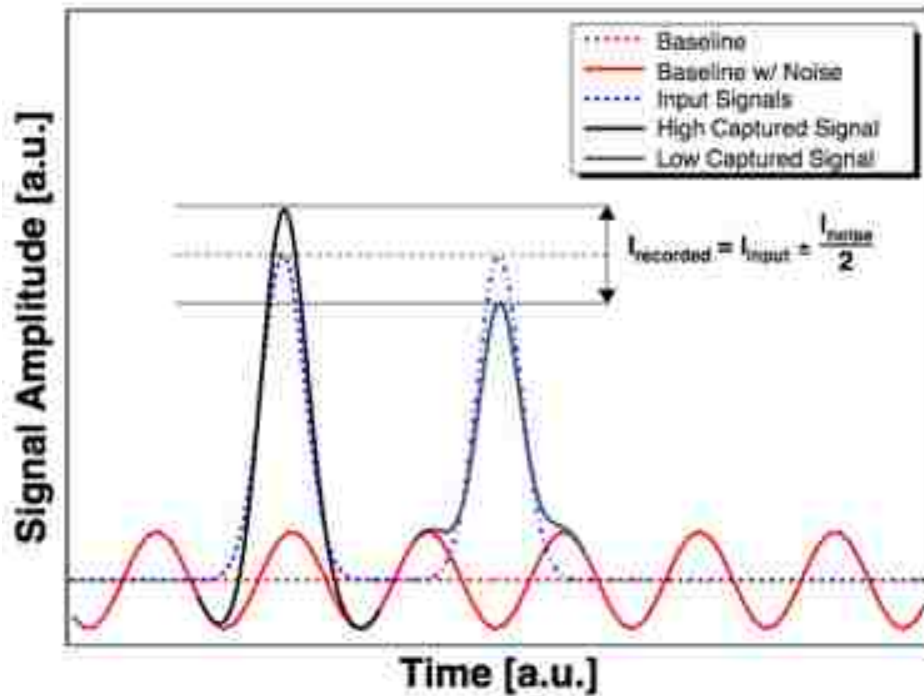
Figure 3.3: Example of common-mode noise on an input signal.

The average pedestal deviation for the 960 silicon pads must be calculated separately from the 42 CsI crystals because it uses an independent power supply and therefore has a different amount of noise. It should also be noted, the average can be calculated for the silicon on the ASIC chip level. Each of the 30 silicon ASIC chips processes signals for 32 detector elements and may experience a different level of noise. CMN correction takes place during pedestal subtraction. To begin the correction, the average deviation from the known pedestal location must be averaged over all detector elements, for each event. The pedestal location for each detector element is known since it was calculated during the pedestal subtraction.

The difference between the recorded signal and the known pedestal centroid is then calculated and averaged over all detector elements, for each recorded signal in the

pedestal only. The method for calculating the average pedestal deviation ($\Delta_{pedestal_j}$) of measurement j is shown in (3.1), where $I_{i,j}$ is the recorded ADC channel for measurement j in detector element i. P_i is the pedestal centroid of element i and n_i is the number of detector elements used in the summation.

$$\Delta_{pedestal_j} = \frac{\sum_i (I_{i,j} - P_i)}{n_i} \tag{3.1}$$

Only signals that are part of the pedestal should be included in the averaging. For this reason a safeguard is placed on the difference $(I_{i,j} - P_i)$ so that only values within $\pm 4\sigma$ of the pedestal are used in the calculation. The average pedestal deviation should be both centered at zero and have a Gaussian shape. Figure 3.4 shows shape of the distribution is Gaussian in both cases, silicon (left) and CsI (right), however neither is centered at zero. A possible explanation is systematic noise among the channels, which likely varies by data set.
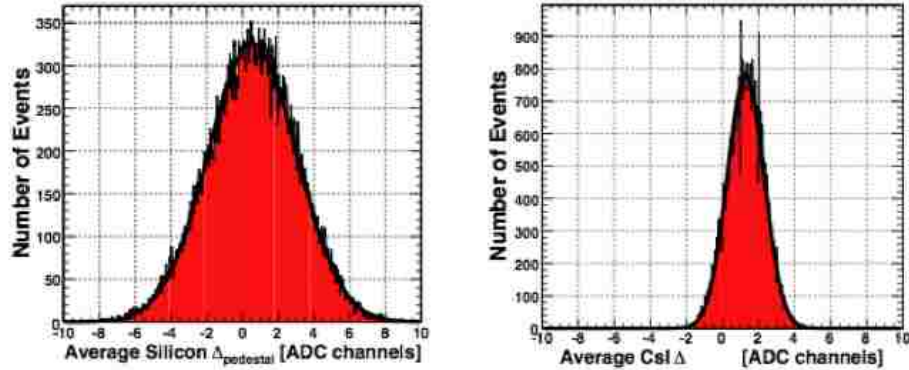
Figure 3.4: Average pedestal deviation distribution for silicon (left) and CsI (right).

Now that the average pedestal deviation for each measured event has been calculated, the correction can be made. For each detector element, the calculated deviation

28

is subtracted from the measured ADC channel value. After making the correction there is a definite improvement in the silicon pedestal width and a modest improvement in the CsI. The un-calibrated spectrum for silicon element 140 is shown in Fig. 3.5. The width of the pedestal is reduced by approximately 15%, a significant improvement. Likewise the un-calibrated spectrum for CsI crystal 2 is shown in Fig. 3.6. The width of the pedestal is only reduced by 2.5%. The large, positive tail on the pedestal implies bad separation between the detector elements with no signal and those with real signals. This results in a mixing of the real signals with the noise. Nevertheless, the CMN correction is used for the CsI detectors.
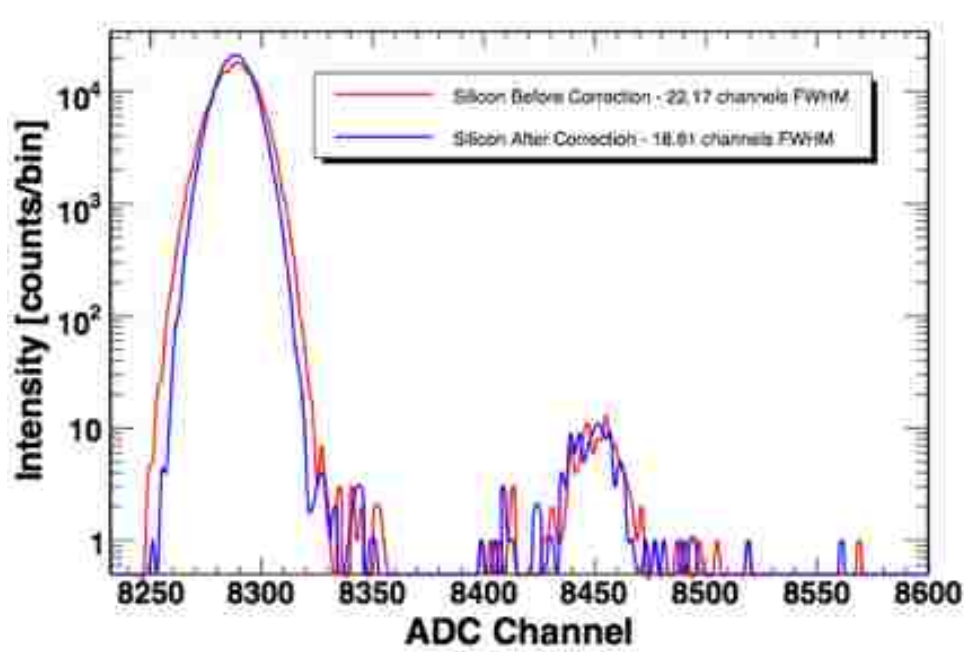
Figure 3.5: Common mode noise correction for silicon element 140 showing a 15% improvement in pedestal width.
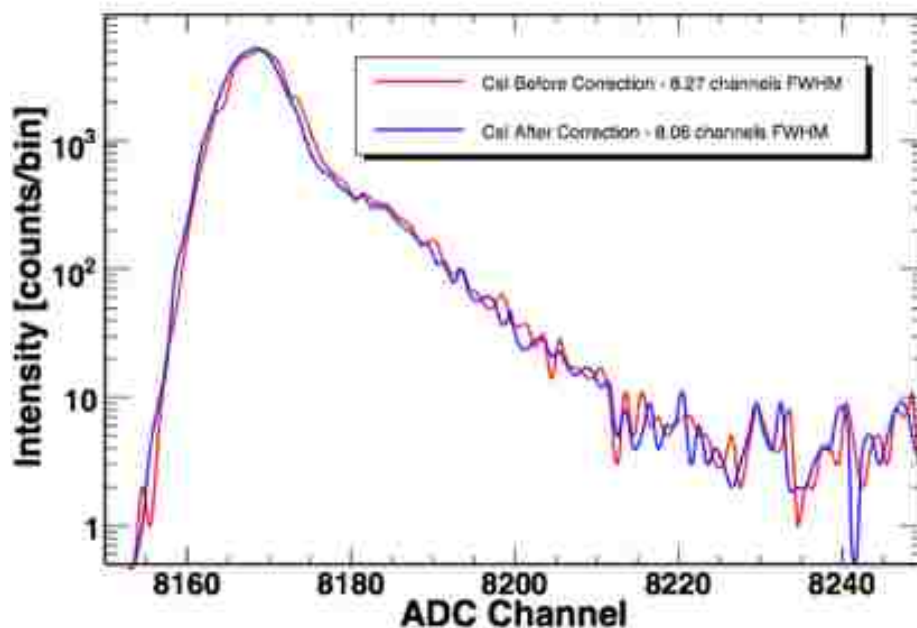
Figure 3.6: Common mode noise correction for CsI crystal 2 showing a 2.5% improvement in pedestal width.

3.3 Energy Calibration

Before any image reconstruction can be performed the ADC channel values of each detector element must be converted to an energy value via calibration. The energy calibration of the silicon detectors must be performed using a low energy check source because the photopeak efficiency of the thin silicon detectors is very low above 300 keV. Calibration of the CsI detector elements must be performed using sources that emit gamma rays at energies higher than 250 keV because of the high hardware thresholds. The three sources used for calibrating the silicon detectors are ^{241}Am, ^{109}Cd and ^{57}Co with gamma-ray emissions at 60, 88 and 122 keV respectively. The CsI was calibrated using ^{137}Cs, ^{54}Mn and ^{22}Na with gamma ray emissions at 662, 834, and 511 and 1275 keV respectively. Table 3.1 summarizes the isotopes and energies

30

used to calibrate both the silicon and CsI elements of the PCI.

Table 3.1: Check sources used for calibration of the PCI.

Source Isotope	Gamma-ray Energy [keV]	Application
^{241}Am	60	Silicon
^{109}Cd	88	Silicon
^{57}Co	122	Silicon
^{137}Cs	662	CsI
^{54}Mn	834	CsI
^{22}Na	511, 1275	CsI

3.3.1 Silicon Calibration

Once sufficient counts have been measured with each of the sources listed in Table 3.1, the known photopeak positions are fit with a Gaussian function for each of the 960 silicon elements. Several checks to ensure proper detector function are also made at this time, for example, a channel that does not have a photopeak is not working correctly and will need to be disabled in the analysis and the trigger for future data taking runs. Also, the resolution of each channel is measured. If the measured resolution is greater than expected, then the channel is automatically disabled and the channel is not used in the calibration. Once all the channels have been fit or discarded for each source, a linear fit is applied and the number of points used in the fit is also recorded. For comparison, a calibration is also performed at the ASIC chip level (32 channels). In the calibration routines there is an option to use the individual pixel calibration values or those for each ASIC chip. A mixed calibration may also be performed *i.e.* if the number of points used in the calibration of a single pixel is less than three, then the chip calibration is used by default.

31

3.3.2 CsI Calibration

Each of the CsI elements is calibrated in the same way as the silicon using the sources listed in Table 3.1. Since there are only 42 CsI elements total, each channel is individually calibrated with a linear fit. Those channels which fail the calibration are automatically disabled.

3.4 Automatic Noise Rejection

Some channels in the silicon or CsI will be noisy due to low thresholds and electronic noise. If a channel is consistently triggering the system due to noise rather than actual photon scatters then the data rate for that channel will be obviously higher than a channel that is not noisy. In order to detect problems such as this, a routine has been added to the data analysis suite that calculates the mean trigger rate and the standard deviation (σ) for all the silicon and CsI detector elements. If any single channel is more than 5σ above the mean it most likely contains noisy data and can be discarded confidently as such.

It is important to remove this noise from the data because it will add unwanted artifacts to reconstructed Compton images. There is no doubt that real events are hidden in the noise of these channels but the overall effect of including these channels in the analysis is a net degradation of the images.

3.5 Most Probable Interaction Depth

When interactions in the CsI are processed in the analysis software the position of the energy deposition is typically assumed to be in the absolute center of the crystal, but that is only an approximation. While using the x and y position of the center of

each crystal is the only reasonable choice, there is a most probable z position based on the energy of the gamma ray incident on the detector that can be used. The most probable z position is a function of material density, thickness and energy. The formula shown in Eq. 3.2 gives the most probable interaction depth in centimeters in a material where the density is ρ in g/cm^3, the total attenuation is A in cm^2/g from Ref. [15] and $\lambda = 1/\rho A$ in cm. For the CsI elements in the PCI, z_0 is 0.0 cm and z_{max} is 1.0 cm. In order to correct the interaction position for the PCI the most probable depth must be calculated for each measured CsI signal. Figure 3.7 shows the output (in cm) of the function given in (3.2) for gamma-ray energies from 0 to 1000 keV where 0 cm represents the front face of the CsI array.

$$< z >= \frac{\int_{z_0}^{z_{max}} z e^{-z/\lambda} dz}{\int_{z_0}^{z_{max}} e^{-z/\lambda} dz} = \frac{\lambda^2 e^{-z/\lambda}((-z/\lambda) - 1)|_{z_0}^{z_{max}}}{-\lambda e^{-z/\lambda}|_{z_0}^{z_{max}}} \tag{3.2}$$
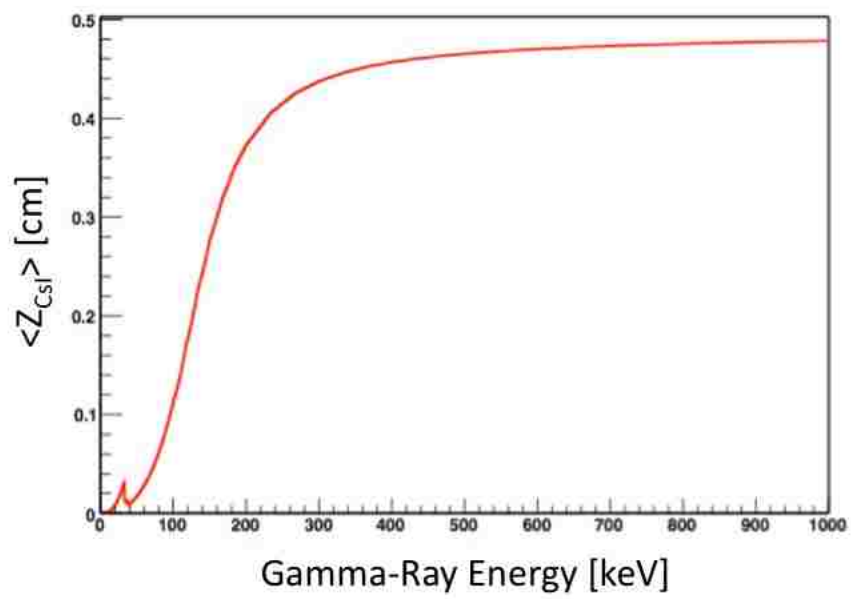
Figure 3.7: Most probable interaction depth in CsI as a function of energy in keV. 0 cm represents the front face of the CsI array.

Chapter 4

SIMULATIONS

The ability to accurately simulate a detector system is critical in understanding the behavior of the detector. Simulations can be used to diagnose problems in the hardware, improve algorithm functionality and allow the user to simulate scenarios that might not be possible in the laboratory. The PCI was modeled using GEANT4 [5], a toolkit for simulating of the passage of radiation through matter. PCI simulations allowed for advanced analysis into the number of interactions which take place in the detector elements and the effects the number of interactions might have on performance. Also, simulations allow for detailed analysis of energy and position resolution effects on angular resolution and once validated can allow the user to test performance gains using different geometries and materials prior to making purchases of expensive components. With a validated simulation toolkit it then becomes possible to confidently model new detector systems prior to construction. This becomes invaluable when designing detectors with time and budget constraints.

4.1 Overview

The PCI [12] was modeled using the GEANT4 simulation toolkit [5]. Doppler broad-ening effects were modeled using the GEANT4 Low-Energy Compton Scattering (G4LECS) package [6], an extension to GEANT4 that accurately models atomic binding effects for low-energy Compton and Rayleigh scattering. When designing a simulation it is important to include all relevant physical processes so that simulated data are as close to measured data as possible. The G4LECS package is important for simulating a Compton imager because it takes into account the fact that electrons involved in Compton scatter interactions are neither free, nor at rest. This is a funda-mental lower limit to the angular resolution of the system and must be included in the simulations. Newer versions of GEANT4 (*4.9.1+*) come "out-of-the-box" with a sim-ilar package to G4LECS called Penelope which has only recently been validated [7]. The use of G4LECS in the future will not be necessary. Figure 4.1 shows the virtual model developed for the PCI using GEANT4.

The model includes all major components of the PCI and any relevant shielding and housings that could cause scattering. In the simulations (as in the PCI), the active area of each silicon plane is divided into 320 pixels, each 3 x 3 mm, and the CsI consists of 42 separate sensors in a 6 x 7 array. The total is therefore 1,002 discrete detector elements. The output of the simulation is a list of detector elements that were hit and corresponding energies deposited in each detector element for a given event. Also included in the simulated output is the exact time of each interaction, the photon vertex and the number and type of interaction that took place. These are helpful data in the analysis of any detector system and can shed light into areas that can be easily improved by hardware or software changes. During analysis, appropriate energy
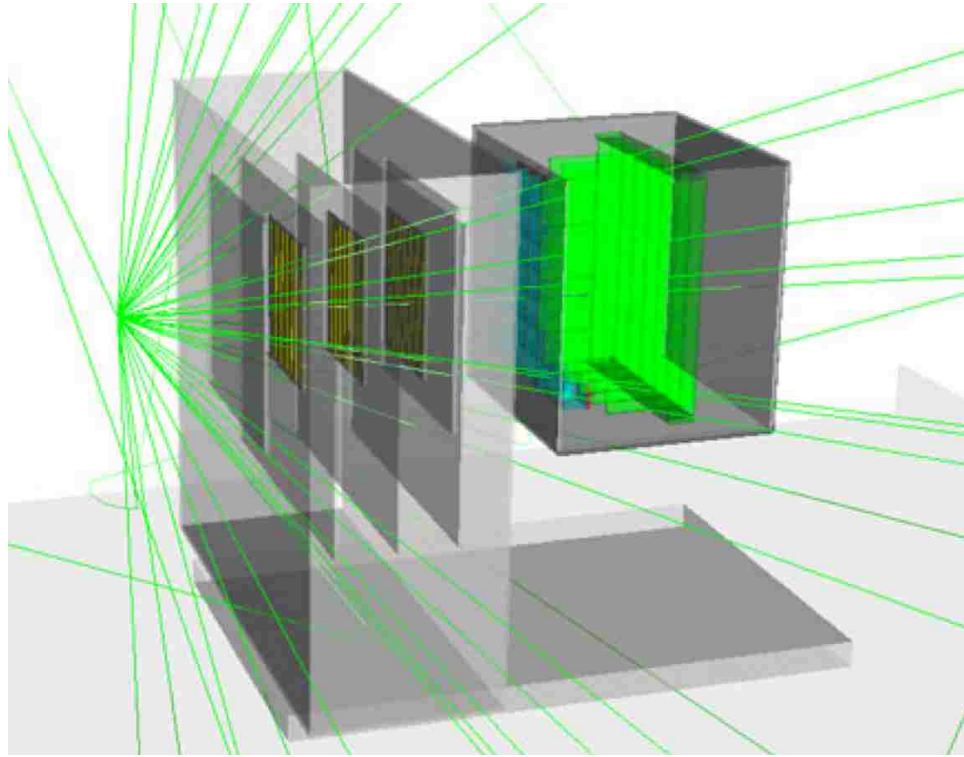
Figure 4.1: Virtual model of the PCI used in the GEANT4 simulations.

resolution is added to the data in order to more accurately model the prototype.

4.2 Resolution Smearing

Output data from the GEANT simulations of the PCI contain exact measurements of energy and position. To validate the simulation, the response of the simulated detector must be compared with the response of the real detector. Before a comparison can be made between measured and simulated data, both position and energy resolution must be added to the simulated data. The ability to add energy resolution to simulated data provides a powerful tool in the analysis of the detector system. For example, testing the effects of energy resolution on a detector system is possible by adding more or

less resolution to the simulated data set. Likewise, position resolution effects can be quantified by increasing or decreasing the size and number of detector elements.

4.2.1 Position Resolution

Although output interaction locations from the simulations are exact, the PCI is only capable of determining which detector element was triggered for a given event. As a result, the exact positions of the simulations must be mapped to the detector element for which it corresponds. In the PCI, each silicon interaction is changed to reflect the center of the active pad that it is mapped to. The CsI interactions are changed to reflect the geometric center in x and y at the most probable interaction depth (z) of the crystal that it is mapped to. The calculation of the most probable interaction depth is shown in Eq. 3.2 of section 3.5. It is also useful to maintain a record of the exact interaction positions to observe the effects of adding position resolution.

4.2.2 Energy Resolution

In order to accurately model the response of any detector, energy resolution consistent with what is expect should be added to simulated data. For the PCI, the energy resolution of the silicon detectors is 36 keV (σ) (coincidence mode) and the energy resolution of the CsI can be described with the function shown in (2.1). For each simulated event, energy is "smeared" using a Gaussian random number generator [28] centered at the exact energy with sigma defined by the resolution function in (2.1). For silicon sigma is assumed to be constant over all energies. Adding resolution makes the energy spectrum appear as through it were observed in a real detector. It is also useful to maintain a record of the exact energy to observe the effects of adding energy resolution. Figure 4.2 shows an example from the PCI simulation of the exact energy

spectrum (red) from a simulated ^{137}Cs source, and the spectrum (blue) of the same data after energy resolution has been added. The photopeak for ^{137}Cs can clearly be seen as a very sharp peak at 661.59 keV in the exact energy spectrum.
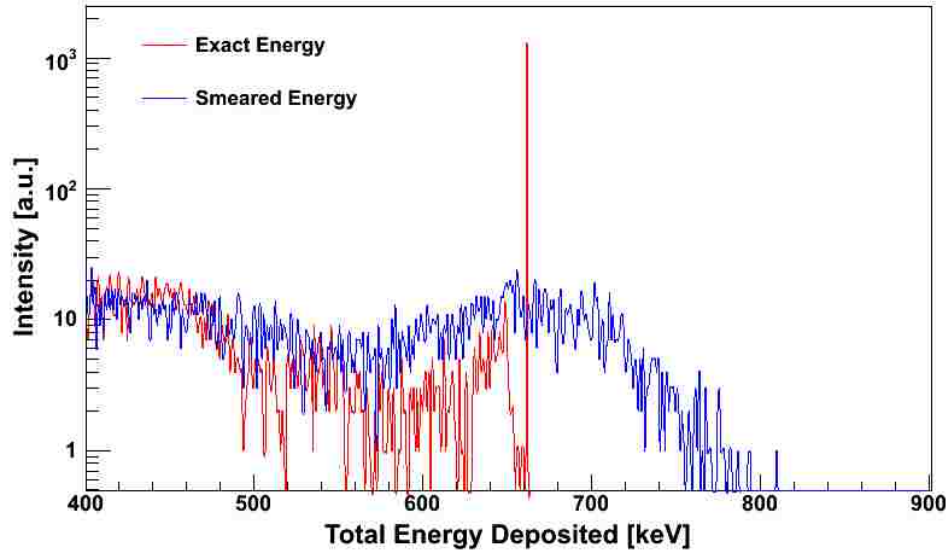
Figure 4.2: Exact energy spectrum of events from a simulated ^{137}Cs source (red) and the spectrum of the same events after energy resolution was added (blue).

4.3   Hardware Threshold

Another aspect that is critical to the operation of the PCI is the energy threshold. If the hardware threshold is set too low, more noise will be allowed to trigger the system and result in poor data quality, if it is set too high some good events will be rejected. The thresholds on the PCI are set sufficiently high to reduce the amount of noise that triggers the system while minimizing good data losses. Since the simulation doesn't include electronic noise it does not need a hardware threshold, so it must be added in post-processing. The hardware threshold is simulated using a random Gaussian function [28]. The function used in the simulated PCI silicon detectors is centered at

52 keV with a width of 15 keV (σ), based on measured data. The function used in the simulated PCI CsI detectors is centered at 400 keV with a width of 100 keV (σ) based on measured data. Figure 4.3 shows simulated ^{137}Cs silicon energy spectrum before and after the simulated hardware threshold is applied. The simulated hardware threshold is applied after energy resolution has been added to the data.
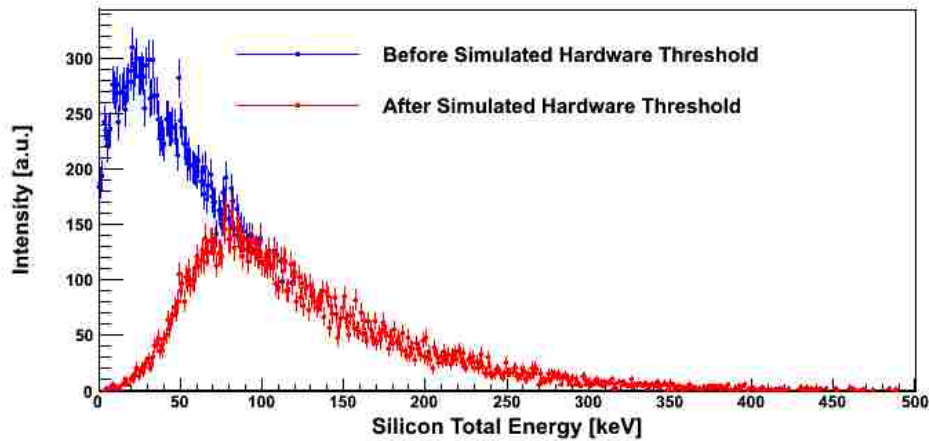
Figure 4.3: Demonstration of the simulated hardware threshold in the silicon detectors.

4.4 Simulation Validation

Now that simulated data have the same position and energy resolution as the PCI, and have a simulated hardware threshold applied, they can be compared to measured data to see if the GEANT4 model of the detector is accurate. Comparisons will be performed on the silicon and CsI energy deposited and the total energy deposited in the system for two-interaction event sequences. This is of interest because two-interaction event sequences are used for imaging. No modeling of the natural background was performed because the rates are very low, typically 0.1 to 2.0 Hz, depending on the

threshold settings and the number of disabled channels. Background contributions in measured data are mostly due to ^{40}K from the concrete in the laboratory and cosmic radiation.

4.4.1 Silicon Energy

Figure 4.4 shows the comparison of measured and simulated silicon energy deposited for a ^{137}Cs source after energy resolution and hardware thresholds have been applied. Measured and simulated data shown in Fig. 4.4 are normalized to the number of recorded events. The simulated and measured results are in good agreement. There is a slight difference in the spectra between 170 and 250 keV, which is likely due to incomplete modeling of objects near the detector, *i.e.* laboratory surroundings.
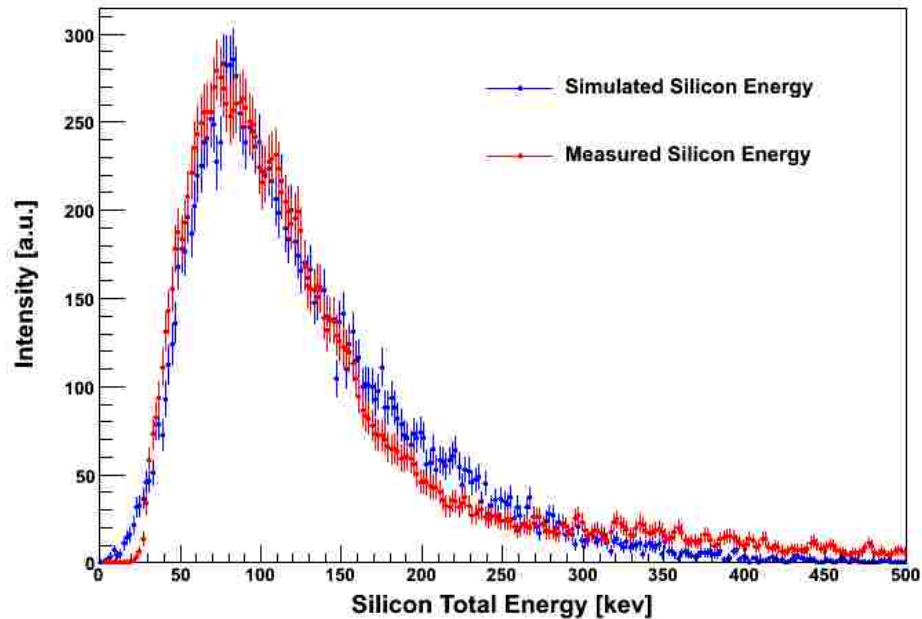
Figure 4.4: Comparison of measured and simulated silicon energy after simulated hardware threshold was applied. These data are normalized to the number of recorded events

4.4.2 CsI Energy

Figure 4.5 shows the comparison of measured and simulated CsI energy deposited for a ^{137}Cs source after energy and position resolution were added and hardware thresholds were applied. It can be seen from the figure that the comparison is very good and the physics model used in the simulation is accurate.
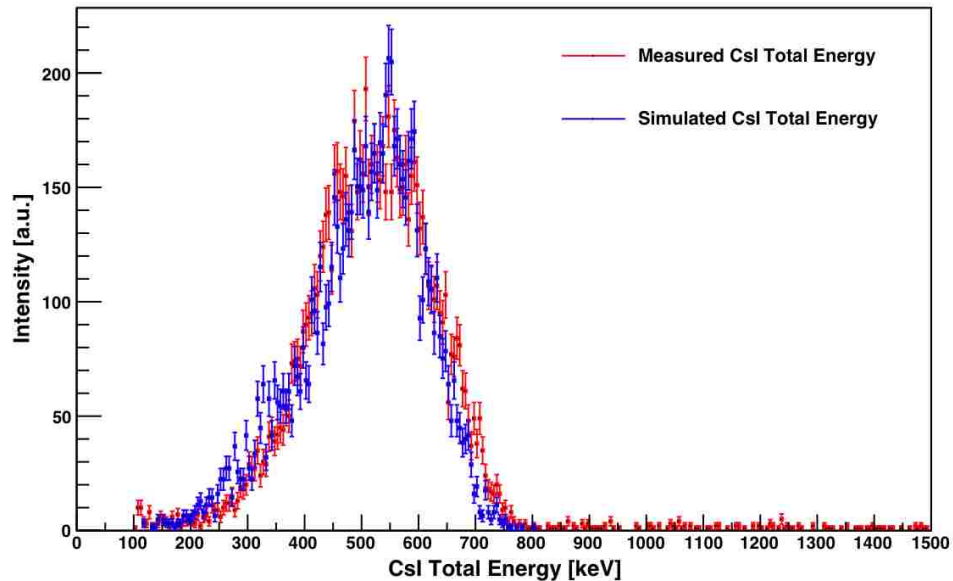
Figure 4.5: Comparison of measured and simulated CsI energy after simulated hardware threshold was applied. These data are normalized to the number of recorded events.

4.4.3 Total Energy

Figure 4.6 shows the comparison of measured and simulated total energy deposited for a single deposition in the silicon scattering detectors and a single deposition in the CsI array. This is the data that will be used for Compton image reconstruction. The high-energy tail on photopeak present in the measured data is from background

which is not simulated. Background was not simulated because the background count

rate is relatively low. Typical background count rates are 0.1 to 2.0 Hz.
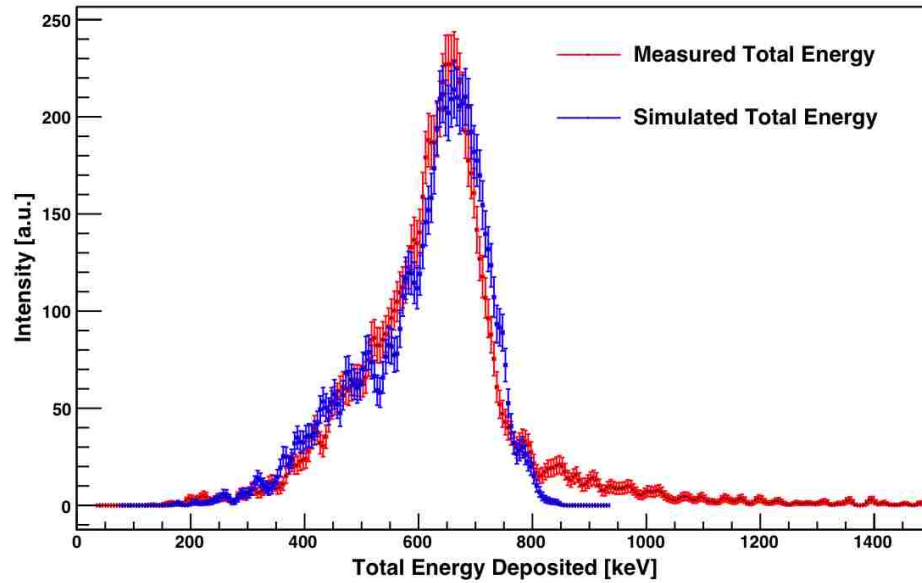
Figure 4.6: Comparison of measured and simulated total energy deposited in the PCI after simulated hardware threshold was applied. These data are normalized to the number of recorded events.

4.4.4   Images

Another important aspect of validating the simulations is to ensure that the simulated images are realistic and reflective of measured data. Figure 4.7 shows an example of a back-projected Compton image produced using measured data (left) and the image produced from simulated data (right). They agree well. Back-projection will be described in more detail in later chapters.
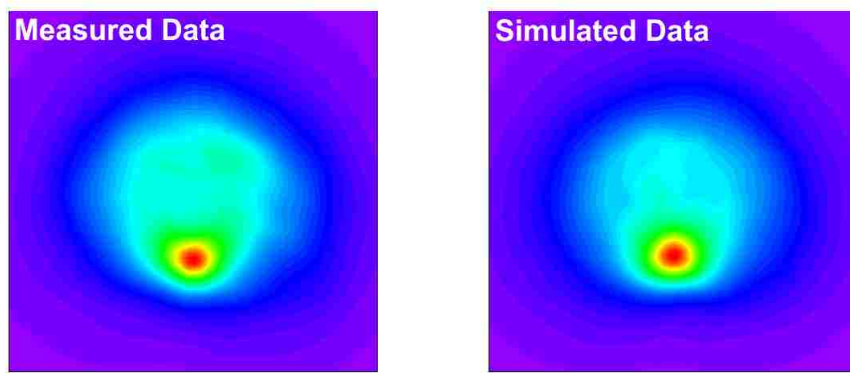
Figure 4.7: Comparison of back-projected Compton images produced from measured (left) and simulated (right) data.

Chapter 5

EVENT RECONSTRUCTION

Reconstruction of a single Compton scatter event requires a minimum of two pairs of energy and position measurements, one pair at the site of the Compton scatter interaction and one pair at the absorption location of the scattered gamma ray. With the recorded energy deposits a scattering angle can be calculated. In the case of the PCI the incident gamma ray energy is assumed to be the sum of all energy deposits. The estimated uncertainty in the scattering angle can be obtained using the known position and energy resolution of the detector system. Both the scattering angle and the uncertainty in the angle are used during image reconstruction. Additionally if the position and energy of the recoil electron can be measured, then more information about the complete event is known and can contribute to the reconstruction, however this is difficult to achieve.

5.1   Scattering Angle

The Compton formula is given again in (5.1) where θ_γ is the scattering angle of the incident gamma ray, E'_e (or E_1) is the energy deposited in the Compton scatter, E'_γ (or E_2) is the energy deposited in the absorption and $m_e c^2$ is the rest mass energy of

an electron (0.511 MeV).

$$\cos\theta_\gamma = 1 + \frac{m_e c^2}{E_e' + E_\gamma'} - \frac{m_e c^2}{E_\gamma'} \tag{5.1}$$

Calculation of the scattering angle from the Compton formula requires knowledge of the incident and scattered gamma ray energies. From the detector, both of these energies are known. For example: a gamma ray Compton scatters causing the electron to recoil with energy E_1 which is stopped in the scattering detector and deposits energy E_1 in it. The scattered photon then gets absorbed in the absorbing detector, depositing energy E_2. The scattered photon energy is E_2 and the total incident gamma-ray energy is $E_1 + E_2$. From the recorded event sequence, the positions of the scatter and absorption are also known. From these positions the direction of the scattered gamma ray can be assumed and the source position can be localized to a point on the surface of a cone. The cone extends out from the scatter position with a central axis defined by the vector between the two interaction positions. The opening angle of the cone is described by the scattering angle and the width of the cone is defined by the uncertainty on the scattering angle.

5.2   Angular Uncertainty

Calculation of the scattering angle alone leads to a thin cone of probability, however the scattering angle has uncertainty associated with it. By including uncertainty in the scattering angle during event reconstruction the cone is given width. By including the width of the cone in reconstruction, the true source distribution can be more accurately described and the imaging algorithms will have a better chance to reconstruct the data correctly. Angular resolution depends on several factors including Doppler

broadening, energy, and position resolution. Doppler broadening represents the lower limit of angular resolution. Even if the energy and position are known exactly, it is not possible to know the initial state of the electron in the scattering medium. Energy and position resolution are known as they are functions of the detector geometry and materials, Their contributions to the angular uncertainty can be calculated for each recorded event sequence.

5.2.1   Position Contribution

Each recorded event sequence includes a list of detector elements that were involved. Since the recorded interaction positions will always have uncertainty associated with them, the contribution to the angular uncertainty due to position uncertainty can be calculated using the following equations (5.2-5.4), in Cartesian coordinates, where θ is the scattering angle, Δx, Δy and Δz are the distances between the two recorded energy deposits in x, y and z respectively. W_x and W_y are the width and height of the detector elements. The silicon pixels are 3 x 3 mm and the CsI crystals are 12 x 14 mm. This calculation may be different depending on the detector system used, it is shown here for the PCI. The silicon detector elements are significantly smaller than the CsI elements, making the size of the CsI elements the dominant contribution to the angular uncertainty with respect to position. In the following equations the size of the silicon pixels is neglected and $W_{x,y}$ correspond to the dimensions of the CsI crystals, where W_x=1.4 cm and W_y=1.2 cm.

$$\sigma_{\theta,position}^2 = \frac{\Delta x^2}{(\Delta x^2 + \Delta y^2)(\Delta z)^2}\sigma_x^2 + \frac{\Delta y^2}{(\Delta x^2 + \Delta y^2)(\Delta z)^2}\sigma_y^2 \qquad (5.2)$$

$$\sigma_{x,y}^2 = \frac{\int_{-W/2}^{W/2} x^2 dx}{\int_{-W/2}^{W/2} dx} = \frac{\frac{x^3}{3}\big|_{-W/2}^{W/2}}{x\big|_{-W/2}^{W/2}} = \frac{W_{x,y}^2}{12} \tag{5.3}$$

$$\sigma_{\theta,position}^2 = \frac{\Delta x^2 W_x^2 + \Delta y^2 W_y^2}{12(\Delta x^2 + \Delta y^2)(\Delta z)^2} \tag{5.4}$$

5.2.2 Energy Contribution

Due to the fact that no detector material has the ability to perfectly resolve the energy deposited, there is additional uncertainty in calculated scattering angle due to finite energy resolution. As with position uncertainty, the energy resolution of the detector system contributes to the reconstructed event uncertainty. To calculate the energy contribution to angular uncertainty, a function describing the energy resolution as a function of deposited energy is needed and can be obtained experimentally. The energy resolution function for the CsI absorbing array in the PCI is shown in (2.1) and the uncertainty in the silicon 36 keV (σ) (see section 2.4.1). Equations (5.5-5.11) show the calculation of the energy resolution contribution to angular uncertainty given the known uncertainty in the energy measurements (σ_{E_1,E_2}).

$$x = 1 + \frac{m_e c^2}{E_1 + E_2} - \frac{m_e c^2}{E_2} \tag{5.5}$$

$$\theta = \cos^{-1} x \tag{5.6}$$

$$\frac{\partial x}{\partial E_1} = -\frac{m_e c^2}{(E_1 + E_2)^2} \tag{5.7}$$

$$\frac{\partial x}{\partial E_2} = \frac{m_e c^2}{E_2^2} - \frac{m_e c^2}{(E_1 + E_2)^2} \tag{5.8}$$

$$\frac{\partial \theta}{\partial x} = \frac{-1}{\sqrt{1 - x^2}} \tag{5.9}$$

$$\frac{\partial \theta}{\partial E_{1,2}} = \frac{\partial \theta}{\partial x} \frac{\partial x}{\partial E_{1,2}} \tag{5.10}$$

$$\sigma_{\theta,energy} = \sqrt{(\frac{\partial \theta}{\partial E_1} \sigma_{E_1})^2 + (\frac{\partial \theta}{\partial E_2} \sigma_{E_2})^2} \tag{5.11}$$

5.2.3 Total Angular Uncertainty

The total angular uncertainty (5.12) is the quadrature sum of the position (5.4) and energy (5.11) contributions. Figure 5.1 illustrates the effect of Doppler broadening and position and energy uncertainty on the total angular uncertainty of the PCI for a ^{137}Cs point source. This figure was created with simulated data where the effect of each contribution was added alone to observe the effect. The angular uncertainty defines the width of the projected cones during imaging.

$$\sigma_{\theta,total} = \sqrt{\sigma_{\theta,position}^2 + \sigma_{\theta,energy}^2} \tag{5.12}$$

5.3 Electron Tracking

Since the silicon detectors in the PCI are relatively thin (270 μm) there is a chance that the recoil electron will have enough energy to exit the silicon plane. If this occurs and the electron passes through the air between the planes without stopping or being
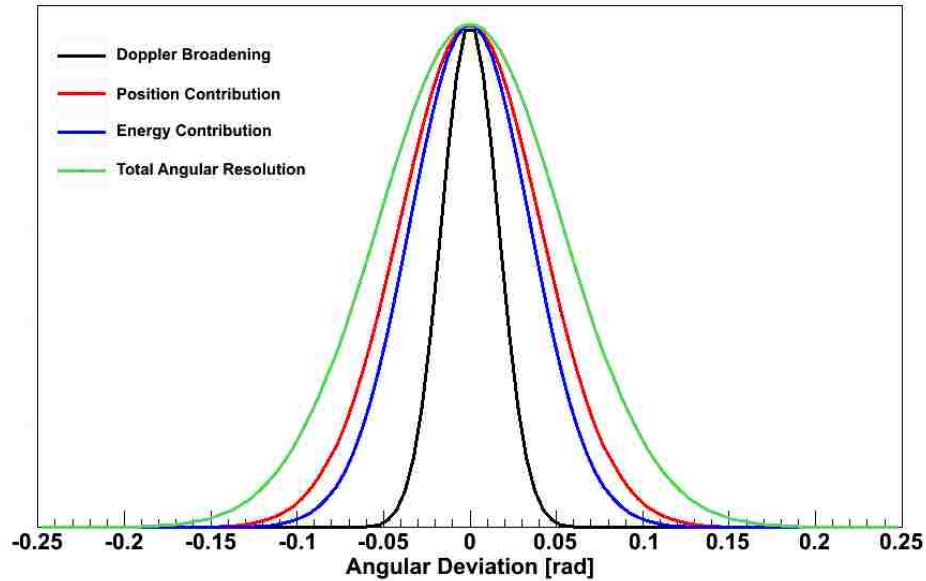
Figure 5.1: Angular uncertainty of the PCI for a ^{137}Cs point source, showing the effects of Doppler broadening and position resolution and energy resolution.

scattered out of the system, the electron can be absorbed in the adjacent silicon plane yielding a second interaction position and another energy deposition. The information obtained from the recoil electron would allow the source location to be reduced from a point on the surface of a complete cone to a point on a smaller arc of the same cone. The momentum vector of the scattered gamma ray can be calculated by multiplying energy deposited in the CsI by the unit vector pointing from the first interaction location in the silicon to the absorption location in the CsI. This assumes that the first interaction happens in one of the silicon planes. The momentum of the recoil electron would be calculated in a similar way but using the first and second silicon interactions and the sum of the silicon energies. Since the total momentum of the system must be conserved, the sum of the scattered gamma ray and recoil electron momentum vectors will give the incident gamma ray momentum vector. In a perfect

50

world the opposite of this vector, starting at the first interaction position, will point directly at the origin of the gamma ray.

Energy resolution will slightly change the momentum vectors and the calculation of the scattering angle leading to an incident gamma ray position that is not quite correct, also the PCI has finite position resolution. Uncertainty in the location of the energy deposits will alter the calculation of the momentum vectors. Also, the recoil electron does not always (or even usually) follow a straight path from the time it is struck by the incident gamma ray to the time it interacts in the adjacent silicon plane. Electron scattering in the path between interaction points can lead to a large amount of uncertainty. Finally, the Compton formula assumes the electron is at rest when the interaction occurs, which it is not. The initial momentum of the electron will alter the kinematics. Since there is no way to know the original momentum of the electron, it cannot be corrected for and the calculated momentum vectors will always have some uncertainty. Once the recoil electron momentum vector is calculated, all that is needed is the azimuthal angle of the vector pointing in that direction. The azimuthal angle of the incident gamma ray along the cone described by the Compton formula can then be calculated as the difference between the azimuthal angles of the scattered gamma and the recoil electron. Some uncertainty must be added to this angle, which results in a section of a cone rather than a complete cone. The size of the section of a cone will be energy dependent.

Studies have shown that while possible, electron tracking is not efficient enough with the PCI to be useful. In order for it to become useful the relative efficiency would have to increase by enlarging the size of the CsI array to allow for more solid angle coverage of the scattered gamma rays and possibly larger silicon active areas

so that more of the escaped recoil electrons could be captured. Also, the thickness of the silicon layers, while small, is not sufficiently small for the recoil electron to escape with a usable probability. Thinner silicon detectors would improve this but would lower the overall efficiency of the system. The hardware thresholds for the silicon and CsI also play a role in the efficiency. Because most of the interactions in the silicon occur at energies well below the current threshold of the system, many, if not most, of the events are being discarded. While this method can reduce the size of the conic section required to reproduce a source distribution, a reduction of 10 to 15 % is not significant, especially when a portion of the cone, likely the section including the reduction, is outside of the field of view of the imaging space. In summary, electron tracking does not help in the image reconstruction for the PCI.

Chapter 6

IMAGING ALGORITHMS

Sufficient information to reconstruct the event cone of a single incident gamma ray can be deduced from a minimum of two position and energy measurements. The next step in the process of Compton imaging is to generate an image based on information collected from many measured gamma rays. The measured distribution of a source will be the intersection of many Compton event cones. Imaging is heavily dependent on two factors: fidelity of the measured data and the qualities of the algorithm employed. Since the fidelity of the data is fixed for a given detector and increased fidelity translates to higher cost, improvements in the algorithms and how they are able to reconstruct the data is of great importance.

There are several methods that yield Compton images. First is back-projection whereby each event cone is projected onto an imaging plane or into an imaging volume. A second method for image reconstruction involves algorithms that perform successive iterations on the back-projected image in order to converge to the most likely source distribution that would have produced the measured data. Both weighted back-projection and maximum likelihood (ML) methods will be discussed in this chapter as well as a method for determining the source-to-detector distance in the near-field

for static (stationary detector) data.

6.1 Geometric Back-projection

Back-projection may be performed in several ways, however in this work a geometric method will be presented because it is fast and accurate. Back-projection involves the reconstruction of a single Compton event sequence onto an imaging plane (2D) or into an imaging volume (3D). The combination of many back-projected event sequences results in the formation of an image. In the geometric back-projection method the definition of the dot product will be used to solve for the intersection points of the event cone and the image pixel or voxel. Begin by supposing that a photon scatters in the detector at point P_1 (x_1, y_1, z_1) and photo-absorbs in the detector at point P_2 (x_2, y_2, z_2). Using event reconstruction, the estimated scattering angle θ and the uncertainty in the scattering angle σ_θ can be calculated (*Chapter 5 - Event Reconstruction*) . The event can then be represented as a cone projected into space from P_1 with its central axis defined by the vector pointing from P_2 to P_1 $(\vec{V}_{21})$ and opening angle described by θ with a width corresponding to σ_θ. Let $\vec{r}$ represent the vector pointing from P_1 along the cone axis to the imaging plane and let $\vec{R}$ represent the vector pointing from P_1 to the intersection point of the event cone and the imaging plane. Figure 6.1 shows the back-projection of a single Compton event sequence.

In order to define $\vec{r}$ (x_0, y_0, z_0), the intersection point of the cone axis and the imaging plane must be calculated. Note that the positions of x_0, y_0 and z_0 represent the center of the image pixel. Larger pixel sizes will decrease the resolution of the image but also decrease reconstruction time. The calculation of $\vec{r}$ is shown in equations
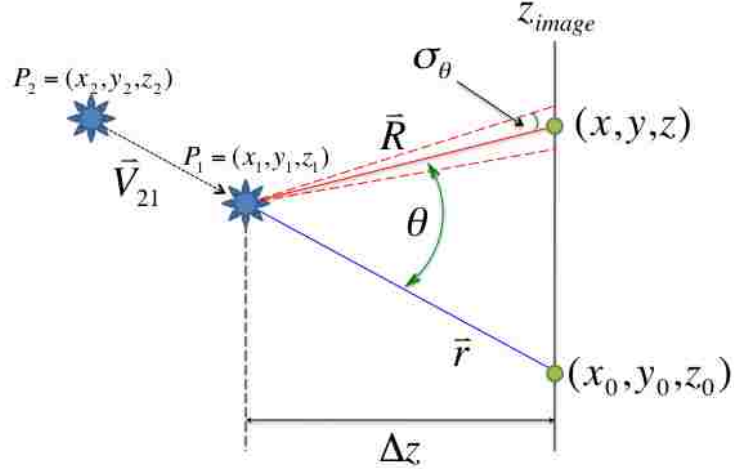
Figure 6.1: Back-projection of a single event sequence.

(6.1 - 6.3) where all coordinates used are shown in Fig. 6.1.

$$z_0 - z_1 = \Delta z \tag{6.1}$$

$$x_0 - x_1 = \frac{x_1 - x_2}{z_1 - z_2}\Delta z \tag{6.2}$$

$$y_0 - y_1 = \frac{y_1 - y_2}{z_1 - z_2}\Delta z \tag{6.3}$$

The back-projection method described here uses the definition of a dot product (6.4) to solve for the intersection of the reconstructed Compton cone and a point in space. Squaring and transposing (6.4) yields (6.5) where the unknown variables of the intersection points (x, y, z) for a given event sequence can be obtained by finding the roots.

$$\vec{r} \cdot \vec{R} = |\vec{r}||\vec{R}|\cos\theta \tag{6.4}$$

55

$$(\vec{r} \cdot \vec{R})^2 - r^2 R^2 \cos^2 \theta = 0 \tag{6.5}$$

Note from Fig. 6.1 that $z_0 = z = z_{image}$. If z is selected as the imaging plane and y is known by selecting a row in the image, then x is the only unknown in the equation. By turning (6.5) into a second order polynomial function of x (6.6), then x can be solved using the quadratic formula (6.7). The coefficients of x are given in(6.8 - 6.10). If the discriminant of (6.7) $(b^2 - 4ac)$ is less than zero it means the cone does not intersect the imaging plane for the selected values of y and z.

$$ax^2 + bx + c = 0 \tag{6.6}$$

$$x = \frac{-b \pm \sqrt{b^2 - 4ac}}{2a} \tag{6.7}$$

$$a = x_0^2 - r^2 \cos^2 \theta \tag{6.8}$$

$$b = 2(x_0 y_0 y + x_0 z^2) \tag{6.9}$$

$$c = y_0^2 y^2 + 2y_0 y z^2 + z^4 - r^2 (y^2 + z^2) \cos^2 \theta \tag{6.10}$$

For any given value of y at a specific z the outside and inside edges of the cone (in x) can be calculated using σ_θ and θ. Pixels between the edges of the cone are filled with weighted values. The result is an event circle scribed onto the imaging plane properly weighted with a width consistent with the limits of the detector.

6.1.1 Cone Weighting

The intersection pixels j of the cone for event i are weighted based on several factors including the width, circumference and the slant of the cone. Weighting the cones is a way to accurately model the information recorded within the event and serves to smooth the images.

In order to account for the width of the cone wall for event i, each pixel j intersected by the cone is weighted according to a Gaussian centered at θ_i with a width of σ_{θ_i}. The formula is shown in (6.11) where θ_i is the computed Compton scattering angle for event i and θ_j is what the scattering angle would be if the gamma ray originated from pixel j.

$$W_{ij,width} = \exp\left[-\left(\frac{\theta_i - \theta_j}{2\sigma_\theta}\right)^2\right] \tag{6.11}$$

The weight for the circumference of the event circle $W_{ij,circ}$, is obtained by dividing the weight by θ_i. This comes from the fact that larger scattering angles result in greater cone circumferences. The weight due to the slant of the cone $W_{ij,slant}$, is accounted for by multiplying by $\cos^3\theta_{\vec{R}}$ where $\theta_{\vec{R}}$ is the polar angle of $\vec{R}$. One power of the cosine term comes from the slant angle of the image area with respect to the event cone and two powers come from the inverse square law.

The total weight W_{ij} of each pixel in the reconstructed event cone is given by the product of all the weights for that pixel (6.12).

$$W_{ij} = (W_{ij,width})(W_{ij,circ})(W_{ij,slant}) \tag{6.12}$$

Figure 6.2 shows a single event cone projected onto an imaging plane and a three-

dimensional view of the same cone to show the weighting of the cone. In the three-dimensional view the weighting due to the cone width and slant are clearly visible.
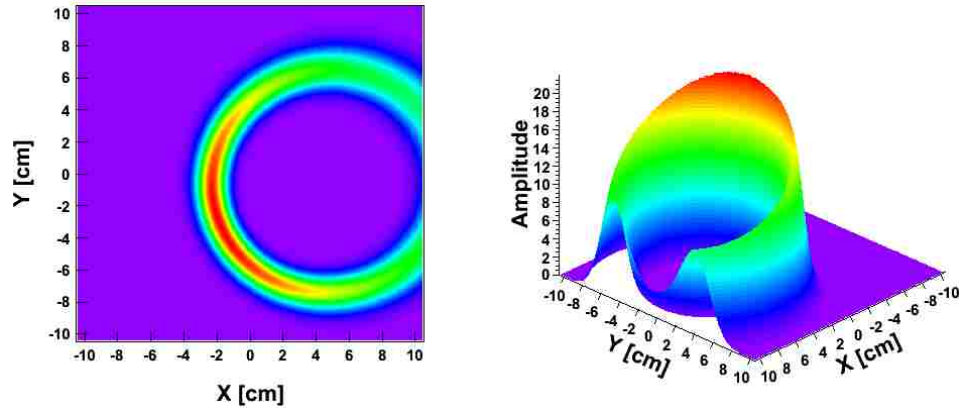
Figure 6.2: A single event cone projected onto the imaging plane (left) and a three-dimensional view of the same cone to show the slant weighting (right).

6.1.2   Image Reconstruction

Back-projection of many cones forms an image, properly weighted on an event-by-event basis. Figure 6.3 shows the sum of 9,876 cones projected onto the same imaging area for a measured, 10 μCi, ^{137}Cs source located at (0.0, -5.0, 9.0) cm where (0.0, 0.0, 0.0) is centered on the silicon detectors along the front face of the bellows.

The image shown in Fig. 6.3 was projected onto a 2D plane at a known z location. The image shown in Fig. 6.3 is of a simple point-like source and it appears that back-projection alone is sufficient to locate the source in x and y. When imaging in the field, the actual imaging distance z may not be known beforehand, therefore a method for determining the depth of the source is presented in section 6.3.

Fig 6.4 shows the image produced via back-projection for an extended source distribution. The source was an "L" shaped source [29] where the length of the long

58
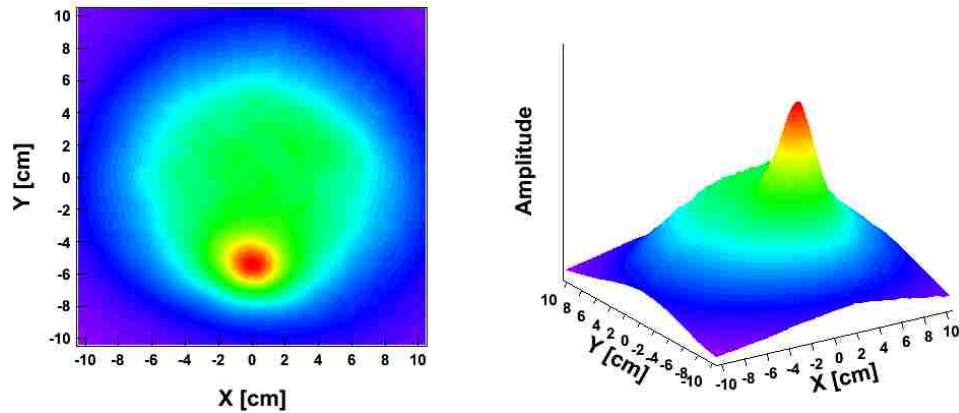
Figure 6.3: Image produced from the sum of 9,876 projected event sequences from a measured 10 μCi, ^{137}Cs source.

(vertical) axis of the "L" was 12.7 cm, the length of the short (horizontal) axis was 5.0 cm, and the width of both the long and short axes was 1.3 cm.

In this case back-projection fails to give any information about the source other than its presence. If the source is not point-like in nature, then the back-projection algorithm has difficulty providing any information about the true distribution of the source. In the event that knowing the shape of the source is necessary, more advanced imaging algorithms must be used. List-mode maximum likelihood expectation maximization (LM-MLEM) is one such algorithm. It has the ability to refine the image produced via back-projection such that more information can be extracted.

6.2 List-Mode Maximum Likelihood Expectation Maximization

Using a minimum of two position and energy measurements the distribution of a source can be reconstructed using many event sequences via the back-projection method. This method works reasonably well for localizing point-like sources, how-
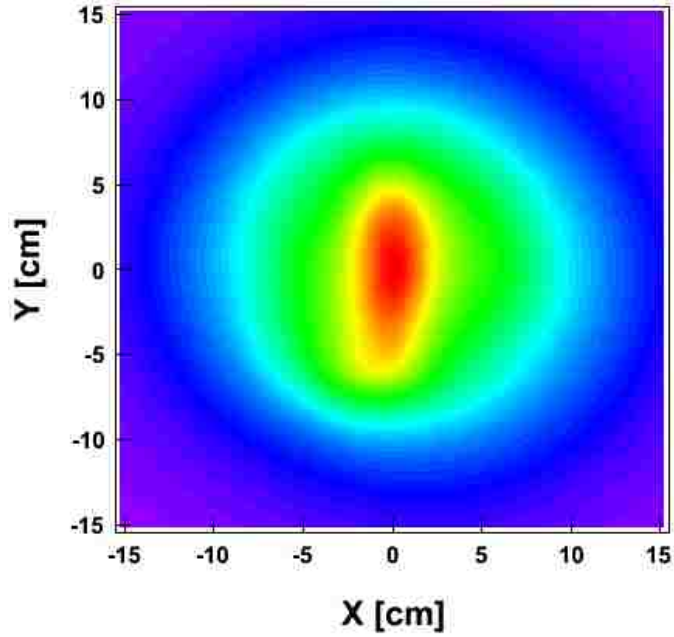
Figure 6.4: Back-projected image of an extended source distribution from the sum of 79,173 event sequences.

ever in the case of a weak source in the presence of a large background or the case of a distributed source, the back-projection algorithm will likely fail to provide adequate deconvolution. List-Mode Maximum Likelihood Expectation Maximization (MLEM) is an iterative statistical algorithm that provides the necessary deconvolution of measured Compton data to resolve distributed sources. MLEM works by attempting to reconstruct the most likely source distribution by finding successive approximations starting from a list of measured events and positions, and a calculation of the expected detector response (system model). List-mode infers that the data being fed to the algorithm is simply a list of N_i energy depositions and interaction points i.e. $i_0 = \{E_1, x_1, y_1, z_1, E_2, x_2, y_2, z_2\}$. From this list, the events can be back-projected in order to obtain a forward model of the data.

6.2.1 Forward Model

Before MLEM iterations can be performed on a data set, the forward model must be calculated using information obtained from back-projection. During back-projection, events are processed, one at a time, into an image. Some of the information obtained in this step needs to be saved in order to be used later by the MLEM algorithm. For each pixel j in the image, the events i with a cone that touched that pixel must be remembered. In addition, for each event i, a list of pixels j in the image that were crossed by that event's cone must be remembered. For example, say the image has $N_j = 100$ pixels, and there are $N_i = 1000$ measured event sequences. For each of the N_j pixels there would be a list of n_i events that touched it, and for each of the N_i events there would be a list of n_j pixels that it touched. These values constitute the forward model.

Once the forward model has been established, iterations begin working backwards, using an update equation, until the data converges upon the most likely source distribution, given the measured data. Since Compton data is inherently noisy, the iterations cannot be allowed to run free until convergence because this will create many artifacts (noise) in the image. Therefore iterations are halted when the variance between the image pixels does not change by more than a predefined threshold.

6.2.2 Update Equation

The update equation for the MLEM algorithm is given in (6.13) [30] where x_j^n is the amplitude of pixel j in the image after n iterations and s_j is the sensitivity of pixel j (from the system model). The main summation is over $i(\cap j)$ or the subset of events i that have a cone that touches pixel j and t_{ij} is the probability of event i being

observed in image pixel j. The second sum is over $k(\cap i)$ or the subset of pixels k that were touched by the cone of event i and t_{ik} is the probability of event i being observed in pixel k.

$$x_j^{n+1} = \frac{x_j^n}{s_j} \sum_{i(\cap j)} \frac{t_{ij}}{\sum_{k(\cap i)} t_{ik} x_k^n} \qquad (6.13)$$

The pixel/event weights (t_{ij}) are calculated as defined in (6.14) where $d\sigma_c/d\Omega$ is the Klein-Nishina differential scattering cross-section [20], R_{12} is the distance between the scatter and absorption locations, θ_{12} is the polar angle of the vector between the scatter and absorption locations, z_2 is the thickness of absorber material as seen from the scatter location and λ_t is the total interaction cross-section evaluated at the scattered energy.

$$t_{ij} = \frac{d\sigma_c}{d\Omega} \times \frac{1 - \exp\left(-z_2/\lambda_t\right)}{R_{12}^2 \cos\theta_{12}} \qquad (6.14)$$

6.2.3 System Model

The system model used in the MLEM algorithm is dependent on the detector and not the algorithm. If the MLEM algorithm is going to be applied to a particular detector system then the system model, or sensitivity function, must be calculated or estimated. Presented here is an analytical method for computing the system model [31].

The system model, or sensitivity, of pixel j (s_j) is calculated analytically before imaging. It is the sum of the probabilities that a single event originating from image pixel j will be detected anywhere in the system. The system model is a function of three position variables (of the source location) and should cover the anticipated

imaging range in x, y, and z.

For each pixel j, the sum of interaction probabilities for each scatter/absorber detector combination must be calculated in order to form the system model. P_0 is defined as the probability that a gamma ray will survive the distance from image pixel j to the scattering location ($R_{j,1}$). P_1 is defined as the probability that a gamma ray will Compton scatter in the thickness of material ($\Delta Z_{scatter}$) as seen from image pixel j. Next, for each possible absorption position, multiplied by the probability P_2 of a gamma ray surviving the distance from the scatter location to the absorption location ($R_{1,2}$), by the probability P_3 that the gamma ray would have scattered in the direction of the absorber element, based on the Klein-Nishina formula [20] and by the probability P_4 that a gamma ray would interact in the thickness of material as seen from the scatter location to the absorption location ($\Delta Z_{absorber}$). The formula for the calculation of the system model is shown in (6.15-6.20).

$$P_0 = \exp\left(-R_{j,scatter}/\Lambda_{air}\right) \tag{6.15}$$

$$P_1 = 1 - \exp\left(-\Delta Z_{scatter}/\Lambda_{scatter}\right) \tag{6.16}$$

$$P_2 = \exp\left(-R_{12}/\Lambda_{air}\right) \tag{6.17}$$

$$P_3 = \frac{d\sigma_c}{d\Omega} \frac{\cos\theta_{12}}{R_{12}^2} \tag{6.18}$$

$$P_4 = 1 - \exp\left(-\Delta Z_{absorber}/\Lambda_{absorber}\right) \tag{6.19}$$

63

$$s_j = \sum_{scatter} (P_0 \times P_1 \times \sum_{absorber} (P_2 \times P_3 \times P_4)) \qquad (6.20)$$

Since only the shape of the function is important, not the overall normalization, all constants are omitted from the calculation. In some cases it may be possible to use a function to approximate the system model. This will save computation time and yield similar results, however a complete calculation should still be performed in order to validate the shape of the function.

Figure 6.5 shows a sample section of the calculated system model for a slice at $z = 10.0$ cm. At any fixed value of z the maximum value for the sensitivity function is at $x{=}0$, $y{=}0$.
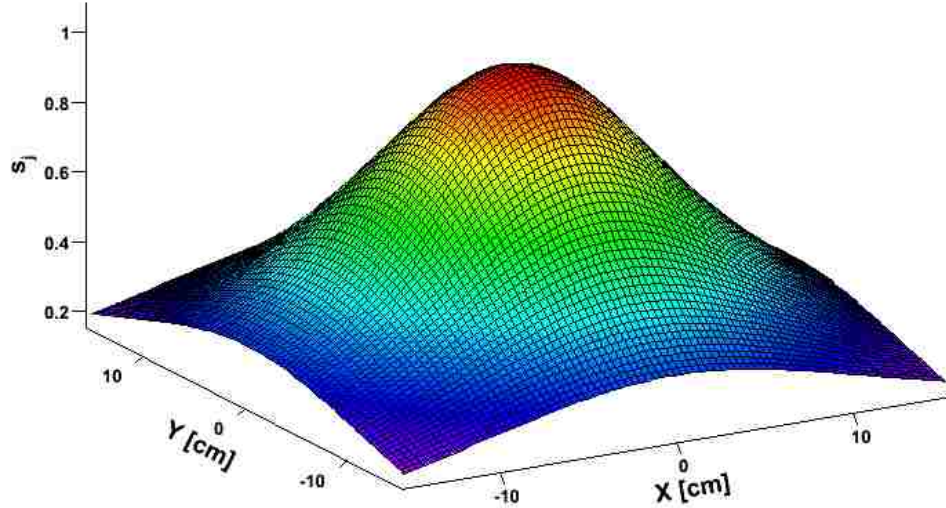
Figure 6.5: Analytically calculated system model at $z = 10.0$ cm. Vertical axis (s_j) gives the normalized probability of detection. The probability of detection is largest (1.0) at $x{=}0.0$, $y{=}0.0$.

Since the method presented here may not be appropriate for all detector systems,

Table 6.1: Comparison of the system model for the analytical, Monte Carlo and functional methods, for the PCI at z=10.0 cm. The model is normalized to 1 at (0.0, 0.0)

Position (cm, cm)	Analytical	Monte Carlo	Approximation $(\cos^{1.75}\theta)$
(0.0, 0.0)	1.00	1.00	1.00
(7.5, 0.0)	0.68	0.73	0.68
(15.0, 0.0)	0.34	0.40	0.36
(7.5, 7.5)	0.52	0.63	0.52
(15.0, 15.0)	0.21	0.25	0.23

one other method for the calculation of the system model is using Monte-Carlo methods where the system model is estimated for many pixels in the image space and then interpolated to form the complete model. A comparison of the analytical solution for the PCI and the Monte-Carlo solution is shown in Table (6.1) as well as a functional approximation.

6.2.4 Source Reconstruction

Extended source imaging was performed with the PCI and an "L" shaped source [29]. The length of the long (vertical) axis of the "L" was 12.7 cm, the length of the short (horizontal) axis was 5.0 cm, and the width of both the long and short axes was 1.3 cm. The source activity was 3616 kBq and it was located at $z = 10.0 \pm 0.3$ cm. The data set contained 275,987 recorded event sequences accumulated over approximately 96 hours.

Figure 6.6A shows the "L" source data reconstructed via back-projection with the actual source position shown with a black line, this is the same image that was shown in Fig. 6.4. It is clear from 6.6A that back-projection is not able to resolve this source. The same "L" source data reconstructed using the MLEM algorithm after 2, 10 and

40 iterations is shown in Figs. 6.6B-D respectively. The shape of the source starts to become apparent after only 10 iterations of the MLEM algorithm.
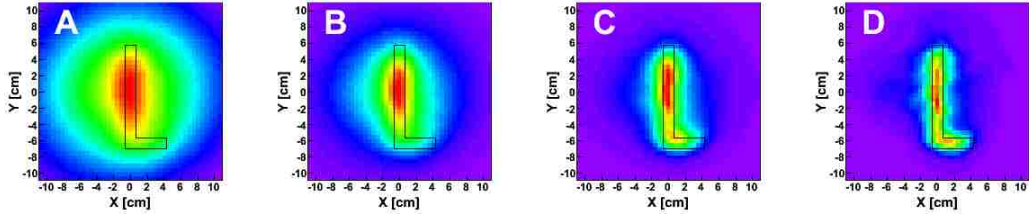
Figure 6.6: Back-projected reconstruction of ^{137}Cs "L" source (A) and MLEM reconstruction after 2, 10 and 40 iterations (B, C, D).

From Fig. 6.6 it can be seen that MLEM is a powerful tool in the deconvolution of Compton scatter data. It is able to improve the fidelity of reconstructed images without changing the measured data.

6.3   Source-to-Detector Distance

So far, images are produced by setting the source-to-detector distance to the known source distance. A method for calculating the source-to-detector distance itself was not investigated. In many applications it is not only necessary to localize a source in a closed volume, with respect to the detector in two dimensions, the source-to-detector distance must also be known. An algorithm is presented here, developed by M.W. Rawool-Sullivan *et al.* [32] for estimating the source-to-detector distance for a point source in a Cartesian coordinate system using only back-projection algorithms. The x and y coordinates of the source can be obtained using the back-projected image and a two-dimensional peak finding algorithm.

The method presented uses the solid angle subtended by the reconstructed images at various source-to-detector distances. The basis for the method lies in the fact that

reconstructed images (in the near field) are of better quality for the 'real' z distance. This is demonstrated in Fig. 6.7 which shows reconstructed images for a point source a various distances. The actual source location was at z=70 mm.
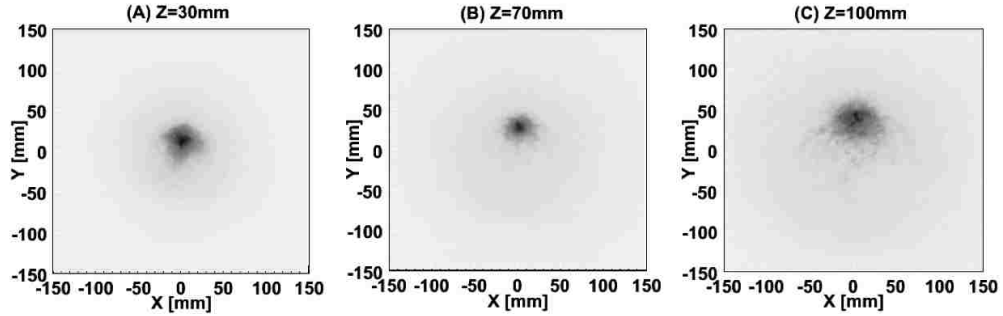
Figure 6.7: Reconstructed images of a source at $x = 10$ mm, $y = 38$ mm, $z = 70$ mm. The image was reconstructed at various source-to-detector distances, $z = 30$ mm (A), 70 mm (B) and 100 mm (C).

The reconstructed image at the correct source-to-detector distance $z = 70$ mm (Fig. 6.7B) is better (i.e. the size of the image is smaller) than for other distances. In addition, when imaging at the incorrect source-to-detector distance, the x and y positions of the source are usually incorrect, with the exception of a located source at $(0, 0)$.

The solid angle subtended by an image is calculated by summing the area of each pixel in the image (A_i) above a certain threshold value, divided by 4π times the distance from the center of the image pixel to the average scattering location of the data set, squared. Equation 6.21 shows the calculation of the solid angle for all pixels above threshold where ΔZ represents the distance between the Compton scatter z (averaged over all interactions) and the center of the imaging pixel and $R^2 = (\Delta X)^2 + (\Delta Y)^2 + (\Delta Z)^2$ where ΔX and ΔY are the distance between the Compton scatter and the imaging pixel for the x and y dimensions respectively. This

expression assumes $A_i \ll R_i^2$, which is a good approximation in this case.

$$\Omega = \sum_i \frac{A_i}{4\pi R_i^2} \tag{6.21}$$

The threshold is defined as the fraction of the maximum single pixel amplitude (MSPA) in the image. For example, a threshold of 0.5 means that all of the pixels whose amplitude is greater than 0.5 times the MSPA in the image will be included in the solid angle calculation. The solid angle subtended by each of the reconstructed images is then plotted against the corresponding source-to-detector distance. As shown in Fig. 6.8, the minimum solid angle subtended (in steradians) corresponds to the correct source-to-detector distance.
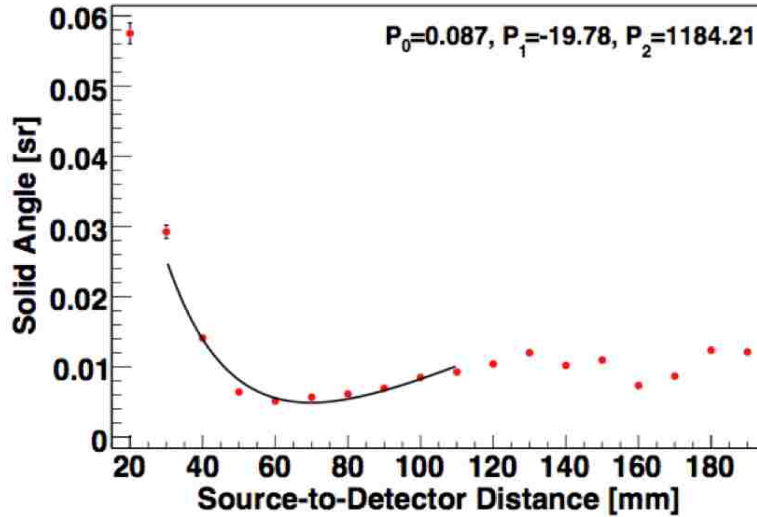
Figure 6.8: Solid angle subtended by the reconstructed image vs. the source-to-detector distance for measured data. The fit to the minimum is shown with a solid line and the threshold was 0.5 MSPA.

An analytic estimate of the solid angle covered by an image with a finite size as a function of Z_{det} results in an expression which depends on Z_{det} as shown in (6.22). Rather than using the exact geometric factors, which give P_0, P_1 and P_2 in (6.22),

68

they are used as parameters in a fit to the data as shown in Fig. 6.8. Taking the first derivative of (6.22) the minimum can be found as shown in (6.23). Propagating the uncertainties on the fit parameters (σ_1, σ_2) through (6.23) gives an estimate on the uncertainty in Z_{min} as shown in (6.24). Here Z_{det} is the distance between the average z location of the Compton scattering interactions (dZ) and the source position (z).

$$\Omega = P_0 + P_1/Z_{det} + P_2/Z_{det}^2 \tag{6.22}$$

$$Z_{min} = (-2P_2/P_1) - dZ \tag{6.23}$$

$$\sigma_{min} = Z_{min}\sqrt{(\sigma_1/P_1)^2 + (\sigma_2/P_2)^2} \tag{6.24}$$

It should be noted that the accuracy of the estimated source-to-detector distance depends on several factors: the statistical uncertainty in the numbers of reconstructed events, peak threshold, pixel size and finite position and energy resolution of the detector system. The effects of angular uncertainty due to energy and position resolution were discussed previously in section 5.2. Out of the remaining parameters, the largest effect comes from limited statistical precision of the image. There are two types of statistical effects. First, statistical uncertainty in the number of reconstructed events, and second the peak threshold which limits the number of pixels used in the calculation. Considering the number of events in the image it is important that any energy windowing of the data (around a photopeak of interest) be made large enough to include all relevant source events while minimizing background and Compton continuum events.

As for peak threshold, a plot of the difference Δz between the actual and the calculated (z) vs. peak threshold is shown in Fig. 6.9. For this particular data set, Z_{min} estimates are relatively stable between threshold values of 0.3 and 0.5 MSPA. In order to better estimate the source-to-detector distance an average is taken over all thresholds between 0.3 and 0.5 MSPA. Because the statistical uncertainties on the points being averaged are correlated, the estimated statistical uncertainty on the average is the average of the error bars of all the points. For the data in Fig. 6.9 the average fit minimum produced an estimated Z_{min} of 70.6 ± 5.4 mm. The actual z in this case was 70 ± 3 mm.
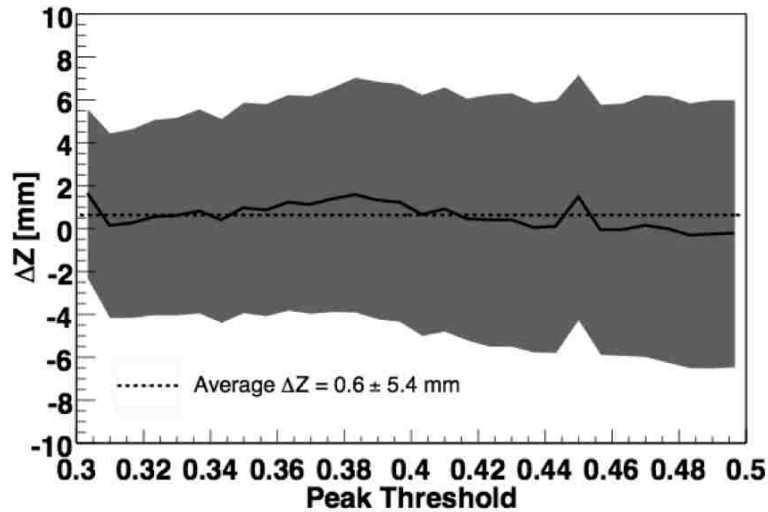
Figure 6.9: The difference between the calculated source z and the actual z position vs. peak threshold. The average Z_{min} was estimated to be 70.6 ± 5.4 mm with a fit between 0.3 and 0.5 MSPA.

Multiple data sets have been analyzed using the technique described here. Results of these experiments are summarized in Table 6.2 and show that this is a simple and effective method for determination of the source-to-detector distance in the near-field.

It has been mentioned several times that this method works in the near-field. If

Table 6.2: Energy and average Z_{min} for three measured data sets.

Source	Incident Energy [keV]	Z_{min} [mm]	Actual z [mm]	Actual x, y [mm]
^{60}Co	1173, 1333	75.9 ± 3.1	80 ± 3	0, -30
^{54}Mn	834	61.8 ± 6.5	70 ± 3	10, 38
^{137}Cs	662	103.2 ± 16.2	100 ± 3	0, -60

source-to-detector distance calculations are needed at much further distances (compared to the transverse size of the detector system) then the imager would have to be mobile in order to give estimates of the source location from many different positions or there would need to be at least two detectors in the field of view of the source with a large separation between them. In the case of astrophysics, where the source is very far away, imaging is performed in angular space and z is assumed to be infinite.

Chapter 7

IMAGING PERFORMANCE

In this section performance of the imaging algorithms developed in this thesis will be demonstrated for a variety of cases including two dimensional imaging of single and multiple point sources and extended source distributions. Two dimensional imaging of point-like sources is perhaps the easiest case for a Compton imager.

7.1   Single Point Source

A single point-like source is the easiest case for Compton imaging. The back-projection algorithm alone should be able to provide the source location in x and y for a given z. The MLEM algorithm may still be applied in this case as a way of increasing the signal to noise and refining the source location. Figure 7.1 shows the reconstructed image of a ^{137}Cs source located (0.0, -6.0, 10.0) cm from the detector origin. This image was reconstructed with the back-projection method described in section 6.1 using 5146 measured event sequences between 600 and 720 keV.

By fitting the image in Fig. 7.1, an estimate of the source location can be found. For this image the source was located at (0.0, -6.1) $\pm$ (2.3, 1.8) cm in x and y, where z is fixed at the imaging distance (z=10.0 cm). The uncertainty in the measured

location comes from the two dimensional Gaussian fit function used.

From the image shown in Fig. 7.1 it can be seen that the back-projection algorithm is sufficient to resolve the image, however applying the MLEM algorithm will serve to further reduce measured position uncertainty in the image location and improve the signal to noise in the image. Figure 7.2 shows the reconstructed image of a ^{137}Cs source located (0.0, -6.0, 10.0) cm from the detector center. This image was reconstructed using 10 iterations of the MLEM method described in section 6.2 using 5146 measured event sequences between 600 and 720 keV. The measured location of the source is now at (0.0, -5.7) $\pm$ (0.9, 0.7) cm in x and y. This shows better than a 50% decrease in the uncertainty of the measured source location.

The angular resolution measurement or ARM distribution of the PCI can be calculated by taking the difference between the scattering angle determined by the energy deposited and the angle between the vector defined by the two measured interaction locations and the vector between the source location and the scattering interaction. The ARM distribution for this source is shown in Fig. 7.3 where the calculated angular resolution is 0.156 radians or 8.94 degrees FWHM, determined using a double Gaussian fit function. The tails of the ARM distribution are the result of incomplete collection of energy in the PCI and incorrect sequencing of events.

These examples show that imaging of a single point source using both the back-projection and MLEM methods is possible and demonstrates excellent source localization and angular resolution. Since the angular resolution of the PCI is a function of the detector element sizes (silicon and CsI) and the distance between the scatter and absorption planes, the ARM could be improved further by increasing the distance between the silicon and CsI, at a cost of reducing the overall efficiency of the system.

7.2 Multiple Point Sources

It has been shown that simple back-projection works well for a single point source in the image field of view (FOV). When multiple sources are in the FOV simultaneously the back-projection cones of each source can contribute to the background of the other sources. Also, if two or more sources are close together the ability to resolve each source individually becomes difficult.

Figure 7.4 (left) shows the back-projected image formed from two measured sources in the FOV separated by 8.9 cm. The first source is ^{137}Cs and was located at (0.0, -5.0) cm. The second source was ^{54}Mn and was located at (1.0, 3.8) cm. Both sources were 7.0 cm from the front of the detector. The two sources are far enough apart that back-projection is able to resolve both sources separately. The imaging algorithm reported the positions of the cesium and manganese sources at (0.1, -4.4) $\pm$ (0.5, 0.5) and (1.2, 3.4) $\pm$ (0.8, 0.9) cm respectively.

As the distance between multiple sources decreases, the ability of the back-projection algorithm to resolve each source is degraded. Figure 7.5 (left) shows two simulated 600 keV point sources separated by 10.0 cm. The back-projection algorithm smears the positions such that they appear to be either two separate sources or a single elongated source. Figure 7.5 (right) shows the same data set after applying 30 iterations of the MLEM algorithm. MLEM in this case was able to provide the deconvolution necessary to remove any ambiguity about the true source distribution.

If the two sources are moved closer, the back-projection algorithm is unable to distinguish between them, however it does at least give an indication that a source might be present. Figure 7.6 (left) shows the back-projected image of two simulated 600 keV point sources located at (-2.0, 0.0) and (2.0, 0.0) cm. In the back-projected

image the sources appear as a single elongated blob along the y-axis. Figure 7.6 also shows the same two sources (right) after applying 30 iterations of the MLEM algorithm. In this case it becomes clear that two distinct sources are present.

In the event of many sources close together in the same FOV, the back-projection algorithm fails to provide any information about the true source distribution. For example, Fig. 7.7 (left) shows the back-projected image of four simulated 400 keV point sources located at (-3, 0), (3, 0), (0, 3) and (0, -3) cm, all at Z=10.0 cm. By applying 200 iterations of the MLEM algorithm it becomes clear that four separate sources are in the FOV at the described positions as shown in Fig. 7.7 (right). The located source positions for the four sources are shown in Table 7.1.

Table 7.1: Located positions and uncertainties of the four simulated sources shown in Fig. 7.7 after 200 iterations of the MLEM algorithm.

Simulated Source Position (cm)	Located Source Position (cm)
(-3.0, 0.0)	(-2.7, 0.0) $\pm$ (0.4, 0.4)
(3.0, 0.0)	(3.0, 0.0) $\pm$ (0.4, 0.4)
(0.0, 3.0)	(0.0, 3.0) $\pm$ (0.4, 0.4)
(0.0, -3.0)	(0.0, -2.7) $\pm$ (0.4, 0.4)

7.3 Extended Sources

Because of the way Compton events are projected there are many pixels in the image that get filled which are not part of the source. During imaging of an extended source distribution the back-projected image becomes convolved with background from true events. This makes it difficult, if not impossible, to determine source location and shape. In this case it becomes clear that a more elaborate algorithm such as MLEM is needed. Extended source imaging with the PCI was performed using two different

source distributions, an "L" shaped source and a ring shaped source. The results of extended source imaging using the PCI were published in [31]

7.3.1 ^{137}Cs "L" Shaped Source

The length of the long (vertical) axis of the "L" was 12.7 cm, the length of the short (horizontal) axis was 5.0 cm and the width of both long and short axes was 1.3 cm. The source activity at the time of measurement was 3616 kBq. The "L" source was located at $z = 10.0 \pm 0.3$ cm. There were 275,987 recorded event sequences, which took a little over 4 days to collect. Of the events that satisfied the hardware trigger condition, only 69,627 were used in the image after energy windowing. Figure 7.8A shows the back-projection reconstruction of the "L" shaped source. It is clear that back-projection alone is not adequate for extended source imaging. Figures 7.8 B and C were reconstructed using the MLEM method. The lines in 7.8C show the actual "L" source source and location.

Figure 7.9 demonstrates the progress of MLEM iterations for the data shown in Fig. 7.8B. Image quality gets better as the number of iterations increases. Iterating past the point of convergence does not improve image quality. For this measured data set, processing was halted after 30 iterations.

Figure 7.10 shows the images that result when a subset of the events used to create the image in 7.9D are used. The four cases shown use 2000, 5000, 10,000 and 69,627 imageable events (after energy windowing). The image becomes better defined as the number of events used increased. It is clear that 2000 events are insufficient and the 5000 events gives only a hint at the true shape. The true shape starts to become clear after 10,000 events and is quite clear after 69,627 events.

7.3.2 ^{54}Mn Ring Source

A ring shaped source was fabricated using a point source and a propeller attached to a motor which rotated at 1 rpm. The shaft of the motor was parallel to the z axis. The point source was attached to one end of the propeller and therefore, averaged over time, produced a ring shaped source with the ring contained in a plane parallel to the xy imaging plane.

The propeller swept out a circle with radius 5.5 $\pm$ 0.2 cm. This approximated a radioactive ring source. The ring source was at $z = 11$ cm. MLEM iterations of measured and simulated ring source data are shown in Figs. 7.11 and 7.12 respectively. Using the MLEM algorithm, the measured and simulated reconstructed images are similar and in both cases the ring-shaped image is reconstructed well. The width of the ring in the reconstructed image is approximately 3.4 cm FWHM. The diameter of the source itself is 0.5 mm – which is small compared to the width of the reconstructed ring. This width is due to the finite resolution of the PCI imager. Figure 7.12 compares an image from the reconstruction of simulated events. Figure 7.12A shows the ring image which would result if the PCI had perfect energy and position resolution. Figures 7.12B and 7.12C are similar to the results of the real data shown in 7.11.
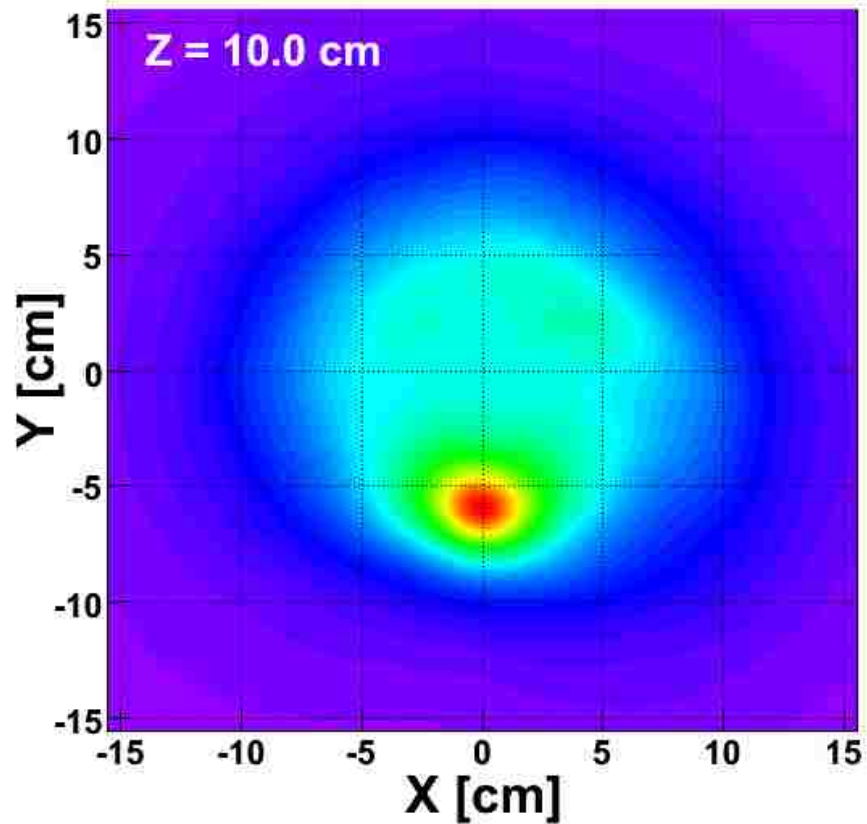
Figure 7.1: The reconstructed image of a ^{137}Cs source located (0.0, -6.0, 10.0) cm from the detector center. This image was reconstructed with the back-projection method described in section 6.1 using 5146 measured event sequences between 600 and 720 keV.
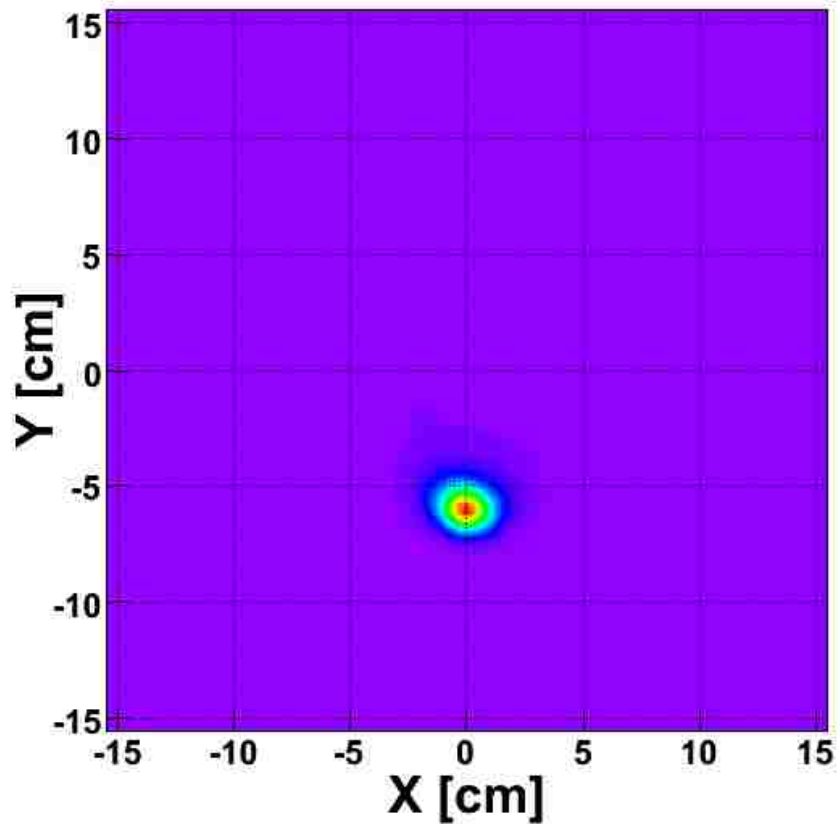
Figure 7.2: The reconstructed image of a ^{137}Cs source located (0.0, -6.0, 10.0) cm from the detector center. This image was reconstructed using 10 iterations of the MLEM method described in section 6.2 using 5146 measured event sequences between 600 and 720 keV.
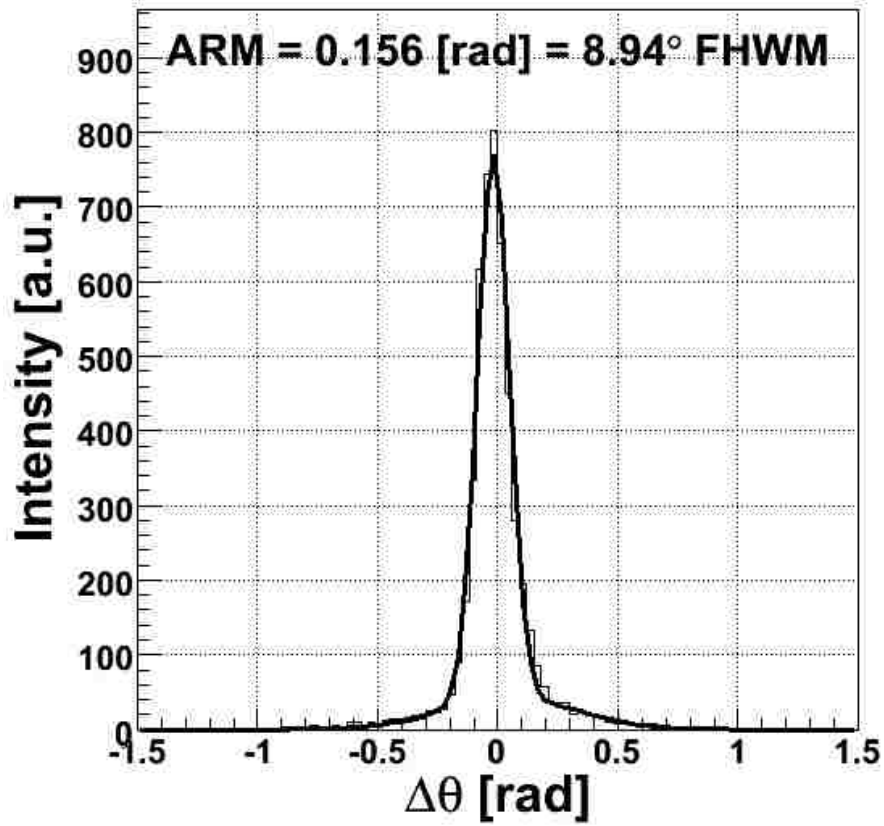
Figure 7.3: Calculated ARM for a ^{137}Cs source at (0.0, -6.0, 10.0) cm. The angular resolution is 0.156 radians or 8.94 degrees FHWM.
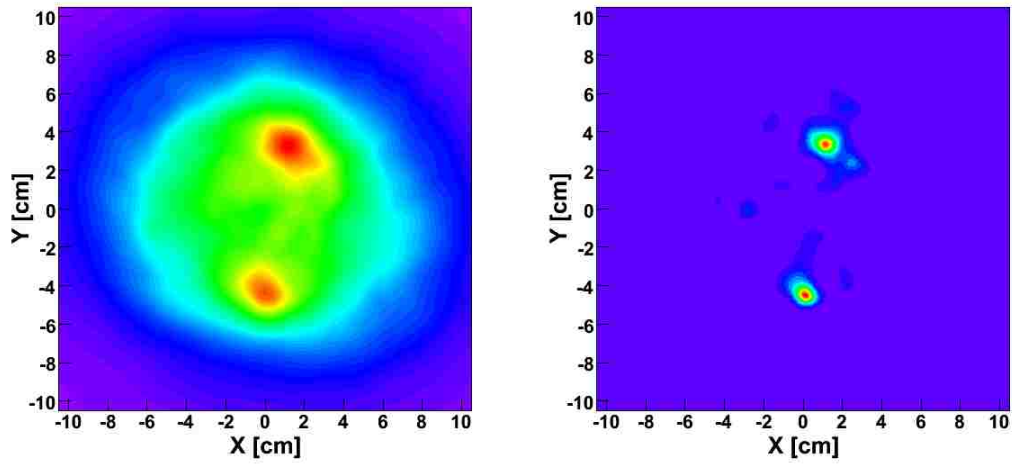
Figure 7.4: Back-projected image of two measured point sources (left) and the same two sources after 30 iterations of the MLEM algorithm (right). The first source is ^{137}Cs located at (0.0, -5.0) cm and the second source was [54]Mn, located at (1.0, 3.8) cm. Both sources were 7.0 cm from the front of the detector.
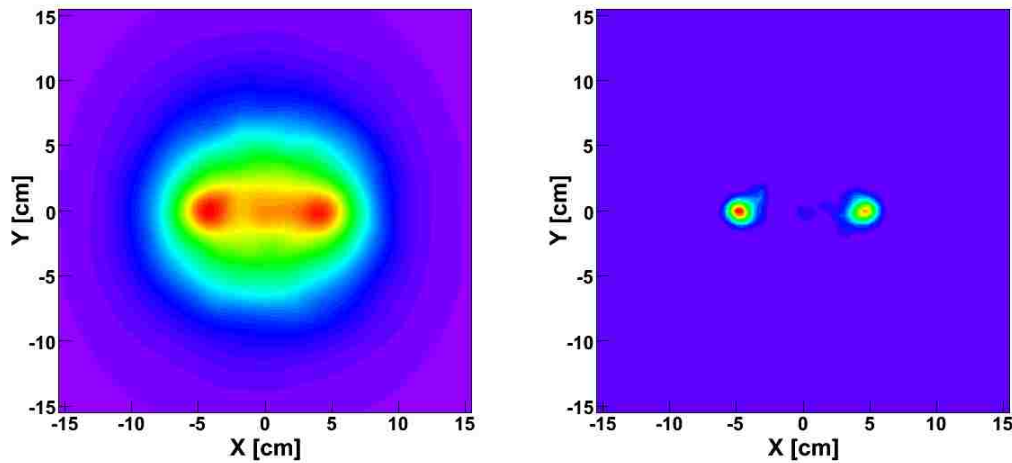

Figure 7.5: Back-projected image of two simulated 600 keV point sources located at (-5.0, 0.0) and (5.0, 0.0) cm (left). The imaging distance for both source was at Z=8.0 cm. The same two sources after 30 iterations of the MLEM algorithm are shown on the right.

Figure 7.6: Back-projected image of two simulated 600 keV point sources located at
(-2, 0), (2, 0) cm (left). The imaging distance for both source was at Z=8.0 cm. The
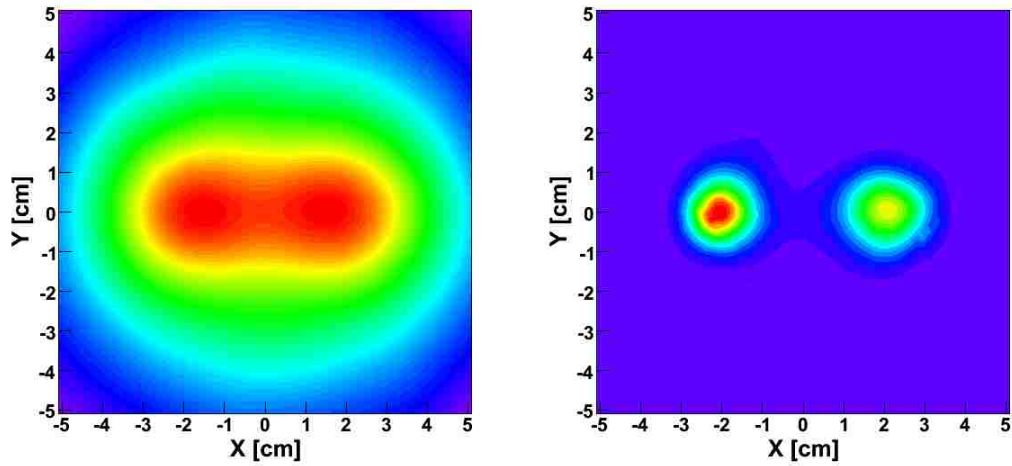same two sources after 30 iterations of the MLEM algorithm are shown on the right.

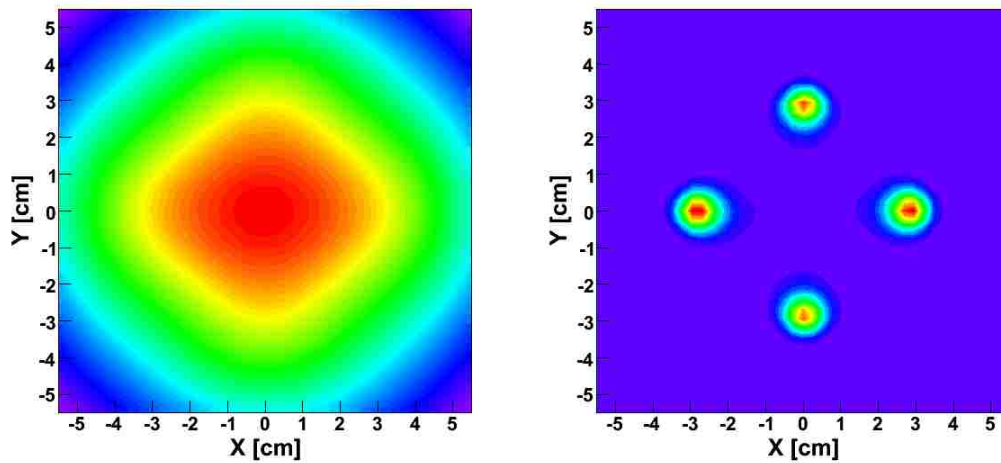

Figure 7.7: Back-projected image of four simulated 400 keV point sources located at
(-3, 0), (3, 0), (0, 3) and (0, -3) cm, all at Z=10.0 cm (left). The same four sources
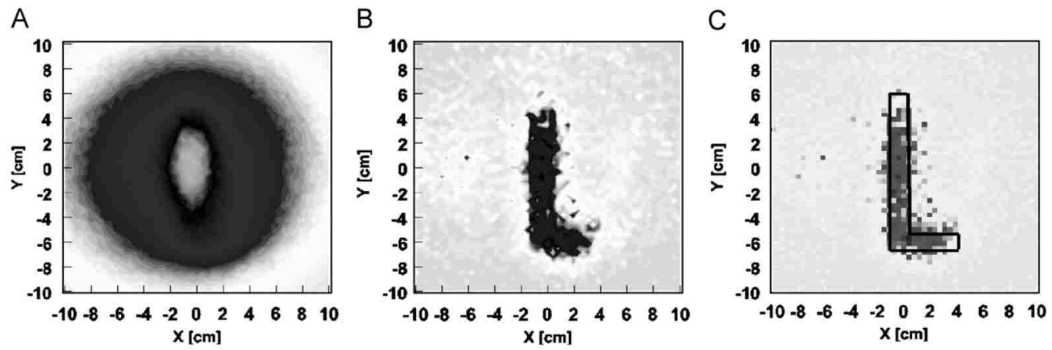after 200 iterations of the MLEM algorithm are shown on the right.

Figure 7.8: A back-projected reconstruction of ^{137}Cs "L" source using 69,627 imageable events (A), a MLEM reconstruction of the same source after 30 iterations (B), and the same MLEM image showing the actual source position (C). The differences between (B) and (C) reflect two methods of displaying the same image. (B) shows contours and (C) shows pixel intensity.
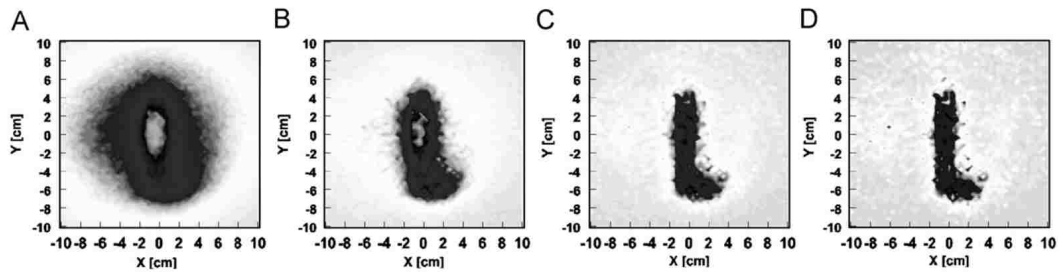
Figure 7.9: The progression of MLEM iterations for an "L shaped ^{137}Cs source. The image after 1 (A), 5 (B), 15 (C), and 30 (D) iterations are shown. These images were generated from measured PCI data.
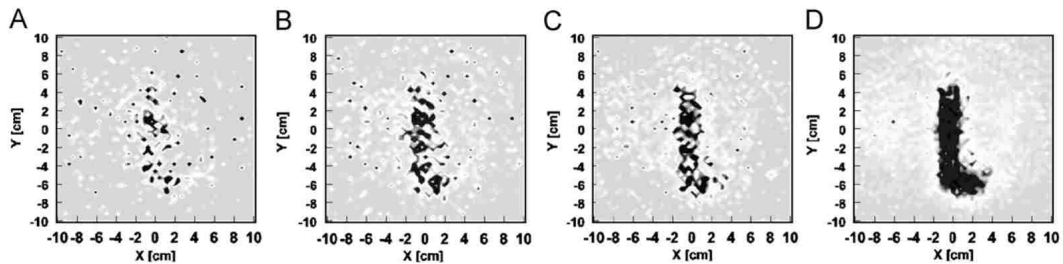

Figure 7.10: Shows the change in the "L-source image as the number of imageable events used is increased from 2000 (A), to 5000 (B), to 10,000 (C), to 69,627 (D). These images were generated from measured PCI data after 30 iterations of MLEM.
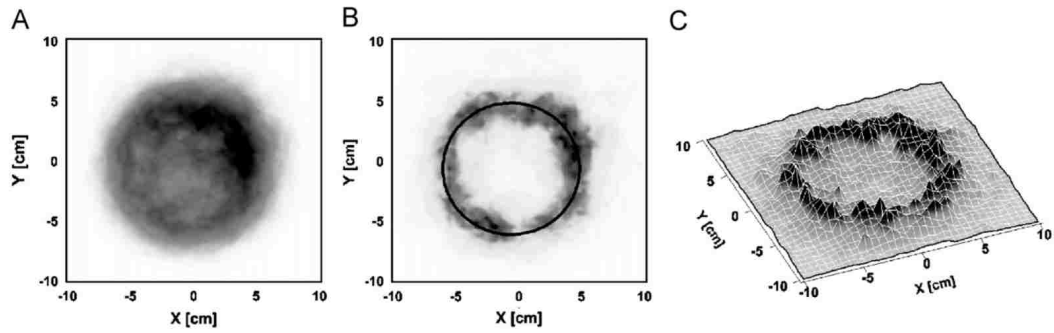
Figure 7.11: Reconstruction of the measured ^{54}Mn ring source data: (A) shows the back-projection image, (B) shows the image after four iterations of MLEM, and (C) shows the image from (B) in a 3D plot. The circle drawn on (B) shows the actual location of the ring source. The center of the circle was at X = -1 cm and Y = 0 cm. The uncertainties on our X, Y and Z measurements in the laboratory were approximately 0.3 cm. The circle drawn has a radius of 5.5 cm. This image consists of 3014 imageable events after energy cuts (790 keV $< E <$ 910 keV). The data set took two days and 4 h to collect
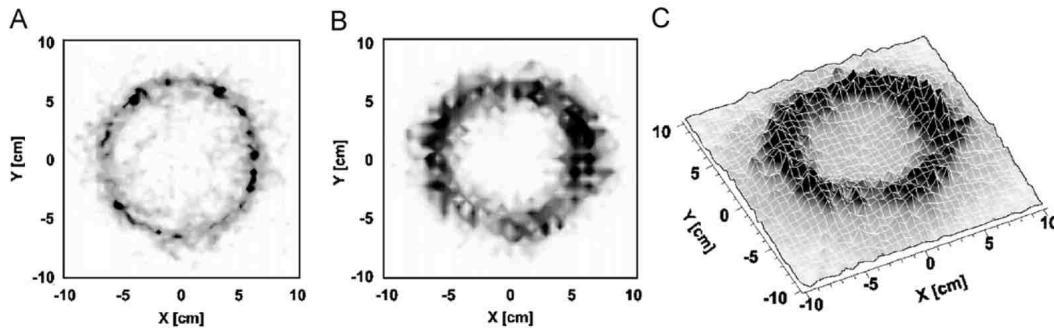

Figure 7.12: Simulated ^{54}Mn ring source before (A) and after (B) energy and position resolution were added. (C) Shows a 3D representation of the ring source with resolution added. Images shown are after four iterations of MLEM. The simulated images use 54,214 imageable events after energy cuts.

Chapter 8

FUTURE WORK

Continuation of this work will follow several paths. First, the algorithms will continue to be developed to provide greater deconvolution at faster processing speeds. The maximum likelihood algorithm will be developed to include full 3D reconstruction of both single and multiple point and extended source distributions. Also, the Compton algorithms and simulation toolkit will be used for future detector development of detection projects such as the Domestic Nuclear Detection Office's (DNDO) Stand-off Radiation Detection System (SORDS) project.

8.1 Three Dimensional Maximum Likelihood

It has been shown that MLEM is an excellent technique that can be applied to Compton imaging. Traditional MLEM is performed in a two dimensional imaging plane, which still requires the knowledge of the source-to-detector distance. It is possible to use the power of the MLEM algorithm to iterate over all three spatial dimensions [34].

Event reconstruction in three dimensions is slightly different than two dimensions. Rather than calculating the intersection of a cone and a plane in space at a fixed source-to-detector distance, events must be projected into an imaging volume as

shown in Fig. 8.1. As in two dimensions the three-dimensional MLEM algorithm will converge on the most probable source distribution. The time required for convergence is heavily dependent on the number of calculations performed per iteration.
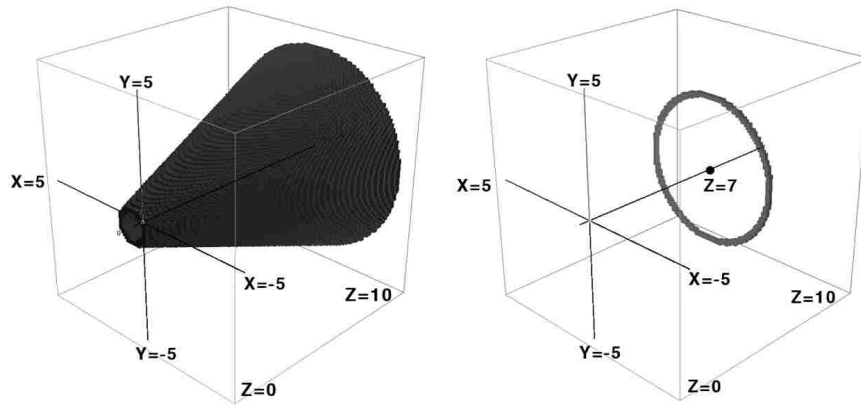

Figure 8.1: Three-dimensional back-projection from Z=-0.5 cm to Z=10.5 cm (left) and two-dimensional back-projection at Z=7.0 cm (right). For both cases X and Y were from -5.5 cm to 5.5 cm. All distances are in centimeters.

In many imaging scenarios the ability to localize a point source in space is crutial and represents the easiest possible case for three-dimensional reconstruction. The next, and somewhat more complex, case of multiple sources may also arise. Here, the ability to distinguish multiple sources from one another becomes important. Sources may also be distributed in x, y or z, further complicating source identification. An algorithm that is capable of handling all of these scenarios is most desirable, and 3DMLEM is one potential path towards this goal. The following three figures show examples of the three cases described. Figure 8.2 shows the 3DMLEM reconstruction of a single ^{137}Cs source measured with the PCI. Figure 8.3 shows both 2 and 5 sources correctly reconstructed from simulated PCI data, and Fig. 8.4 shows a 400 keV simulated line source reconstructed in full 3D.
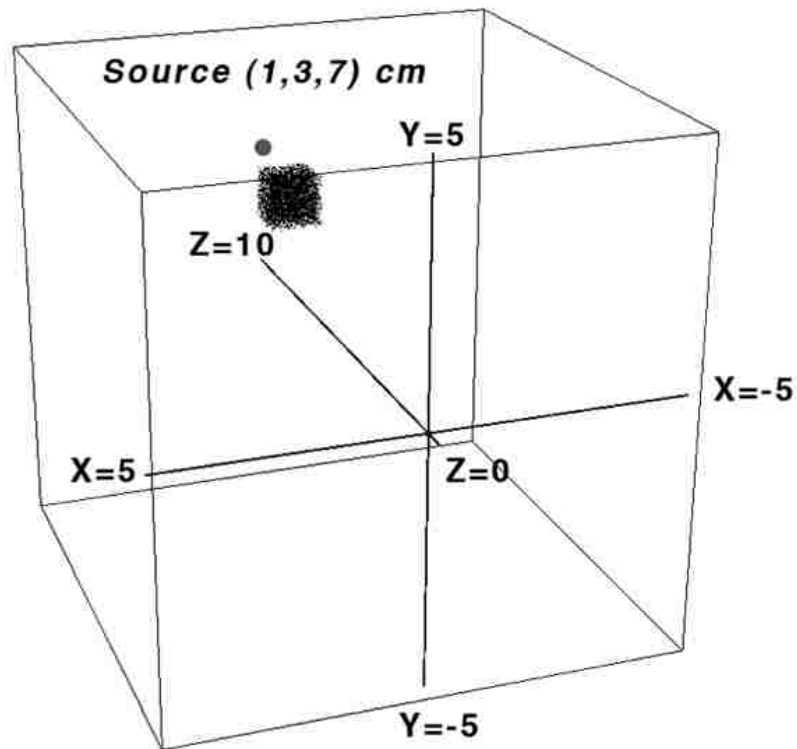
Figure 8.2: Measured data taken with the PCI. ^{137}Cs source located at (1.0, 3.8, 7.0) cm ± 3 mm in any direction. The reconstructed source voxel was located at (1.0, 4.0, 6.0) cm. All distances are in centimeters.

The 3DMLEM method of imaging has been demonstrated in three cases using both measured and simulated data from the PCI. The algorithm currently applies to single point sources, multiple point sources and distributed sources. With more work the flexibility of this algorithm can be improved and demonstrated in a wider range of scenarios.

Figure 8.3: Two simulated ^{137}Cs sources after 50 iterations of 3DMLEM (A). Sources are located and reconstructed at (-1.0, 0.0, 5.0) cm and (1.0, 0.0, 5.0) cm. Five (5) simulated $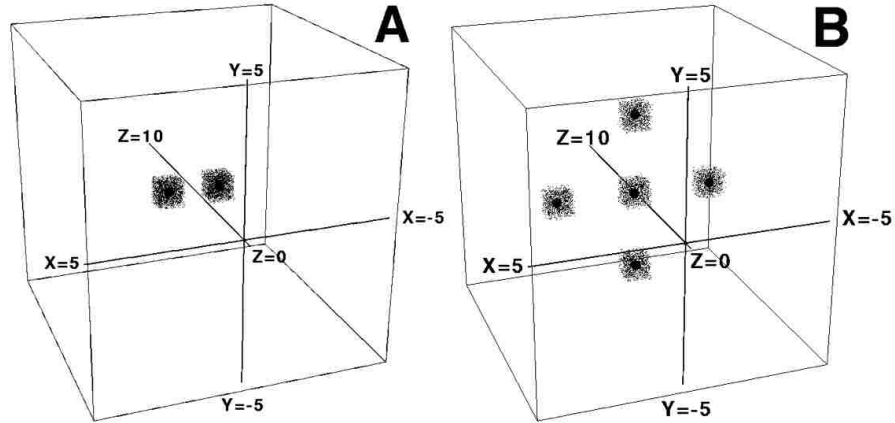^{137}$Cs point sources after 50 iterations of 3DMLEM (B). Sources are located at (0.0, 0.0, 5.0) cm, (3.0, 0.0, 5.0) cm, (0.0, 3.0, 5.0) cm, (-3.0, 0.0, 5.0) cm and (0.0, -3.0, 5.0) cm. All distances are in centimeters.

8.2   The SORDS Tri-modal Imager

The SORDS trimodal imager (TMI) is a gamma-ray imaging device designed to locate and identify threat point sources of radiation from a moving platform [35,36]. Because such point sources will typically be embedded in a background of naturally occurring radiation covering a similar energy spectrum, some means must be applied to separate sources from background. The system is designed to be capable of of imaging both low-energy (<1 MeV) and high-energy (1-3 MeV) gamma rays using three imaging modalities: Compton imaging (CI), coded aperture imaging (CA) [37,38] and shadow imaging. The capability of the TMI to achieve both CI and CA imaging is through the use of active, rather than passive, mask elements in the coded aperture array.

The TMI achieves hybrid imaging by using active mask elements [36]. Photons which interact in both an active mask element and the absorbing back detector are
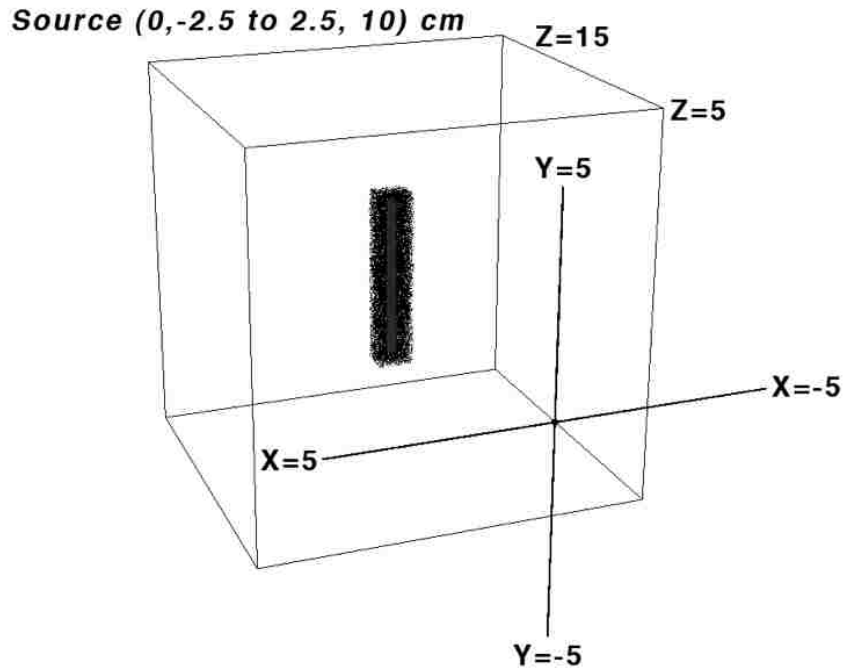
Figure 8.4: Simulated 400 keV line source at z=10.0 cm, centered in x and ranging from -2.5 cm to 2.5 cm in y after 75 iterations of 3DMLEM. All distances are in centimeters.

treated as CI events, while photons interacting in only the back detector are treated as CA events. A variety of means might be used to fuse the two information sources. Fusing the two imaging modalities takes advantage of the fact that the background is imaged differently in the two modes whereas the point source is the same. Figure 8.5 shows an illustration of the TMI truck model used for imaging development.

The front TMI detectors are 5 x 5 x 2 inch NaI(Tl) crystals and the back detectors are 2.5 x 3 x 24 inch NaI(Tl) bars. Position resolution of about 1.85 inches (FHWM @ 662 keV) along the length of the bars is achieved by charge division [36]. Models of the detectors' physical structure and energy resolution were created for both the front and back detectors. Much of the development and testing of the imaging meth-
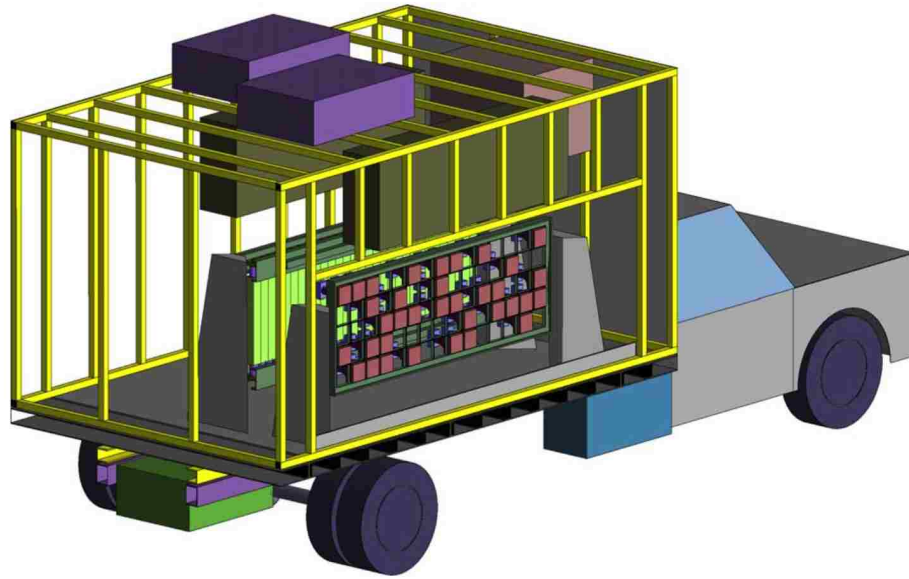
89

Figure 8.5: Illustration of the TMI truck model used for imaging development.

ods and behavior of the TMI were performed using simulation methods similar to the validated PCI model. Results from these models are shown in Fig. 8.6 showing excellent agreement between experimental and simulated data for both front and back detectors.

Also important in the TMI simulation model is the accurate model of background. To this end, a detailed model was developed for a 0.5 meter deep volume of soil of uniform density (1.5 g/cm^3) with the 100 most intense gamma-ray lines propagated out. In order to validate the soil model a simple mass model was created to match the detector configuration for existing background data. Figure 8.7 shows the comparison of the simulated background and measured background from the real TMI truck. In this figure there is no arbitrary scaling of the data, showing excellent agreement. The ^{40}K line is slightly higher in the simulated data, as the natural background rate varies from the averages taken from around the United States used to develop the model.
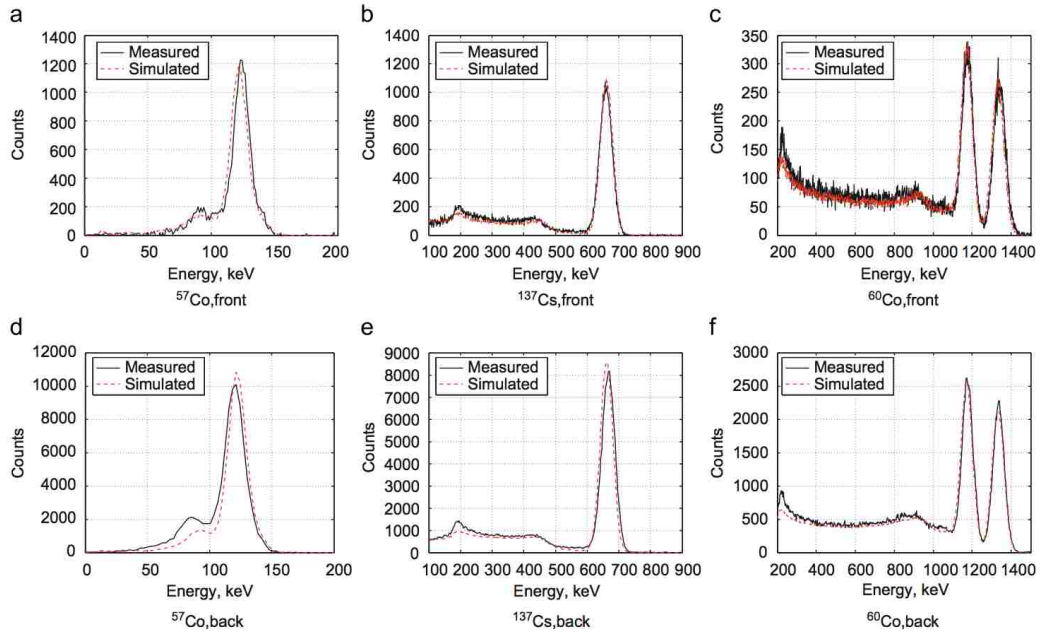
90

Figure 8.6: Validation of TMI detector simulations.

The purpose of the TMI is to locate and identify threat sources while the truck-mounted system is moving. Preliminary testing of the system demonstrates the ability to detect sources while moving. Figure 8.8 shows the reconstructed image of an 876 μCi ^{137}Cs source at 75 m closest approach with the TMI moving at 7 mph. No axes are shown on the image because they correspond to arbitrary row and column numbers in the three dimensional imaging space. Positions of the pixels are relative to the first imaged event. The actual position of a source is reported in geo-coordinates (latitude, longitude and altitude). Figure 8.9 shows the actual path and location of the detected source. The square symbol represents the average location of the TMI for the data used to image the source. The circle denoting the isotope (^{137}Cs) is the reported geo-location and the path of travel is shown with the truck model. The shaded area shows the region of data used to image the source.
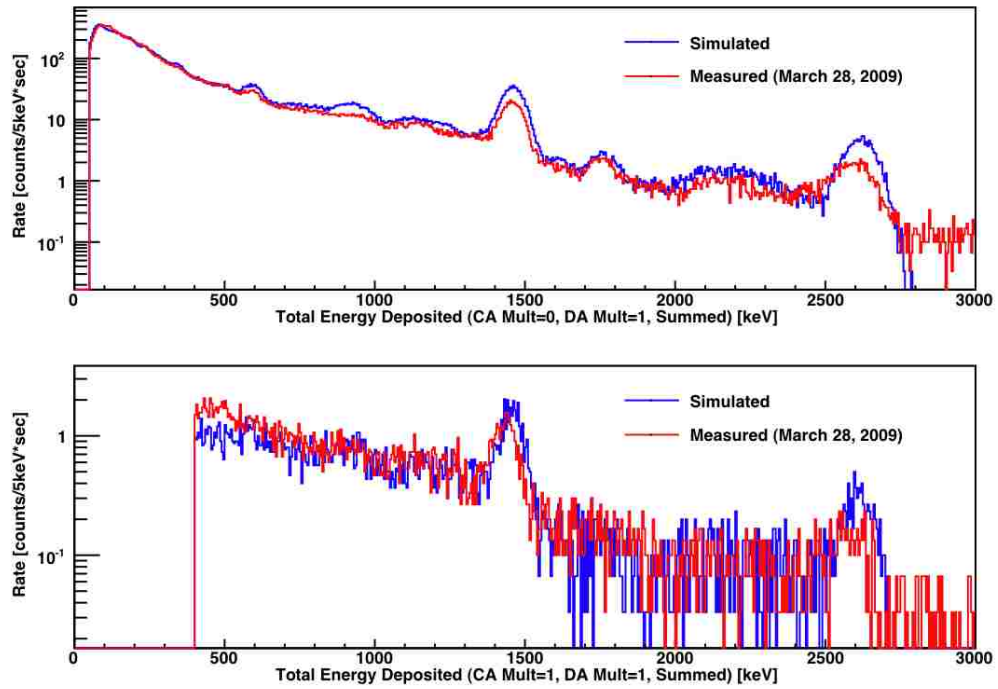
Figure 8.7: Comparison of measured and simulated background spectra for both CA and CI data sets. No arbitrary scaling.
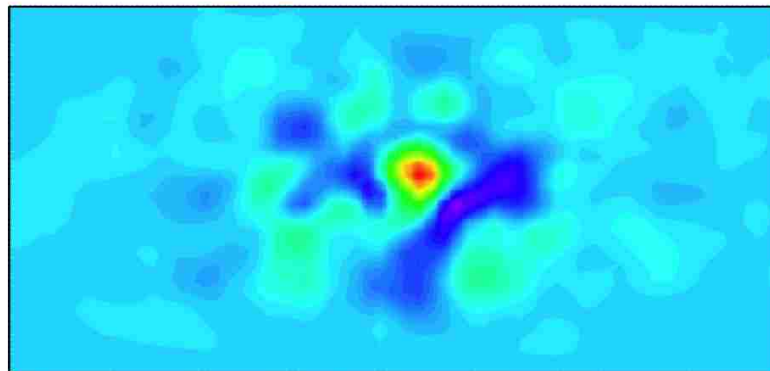
Figure 8.8: Reconstructed 876 μCi, ^{137}Cs source at 75 m closest approach and 7 mph. The lack of axis is explained in the text.

Figure 8.9: Google earth view of the located and identified source. The square symbol represents the average location of the TMI for the data used to image the source. The circle denoting the isotope (^{137}Cs) is the reported geo-location and the path of travel is shown with the truck model. The shaded area shows the region of data used to image the source.

Chapter 9

CONCLUSIONS

Simulations of an existing prototype Compton imager have been performed and validated. They can be used to investigate the efficiency and performance of future instruments. Measurements taken with the prototype have demonstrated the ability to image single and multiple, point-like sources as well as complex extended source distributions with the help of advanced imaging algorithms. The angular resolution of the system was measured to be 0.156 radians FWHM (8.94°). An algorithm to determine the near field source-to-detector distance has been developed and demonstrated. Improved back-projection algorithms as well as maximum likelihood algorithms have been developed and demonstrated to aid in both point-like and extended source imaging. Future work will include continued development of the algorithms presented in this thesis as well as applying the simulation and analysis techniques learned.

Bibliography

[1] J.D. Kurfess *et al.*, "An Advanced Compton Telescope Based on Thick, Position-Sensitive Solid-State Detectors," *New Astronomy Reviews., vol. 48, 2004* pp. 293-298.

[2] L. Mihailescu *et al.*, "SPEIR: a Ge Compton Camera," *Nuclear Instruments and Methods in Physics Research, Section A (Accellerators, Spectrometers, Detectors and Associated Equipment), vol. 570, no. 1, 2007* pp. 89-100.

[3] K. Vetter *et al.*, "High-sensitivity Compton imaging with position sensitive Si and Ge detectors, *Nuclear Instruments and Methods in Physics Research, Section A (Accelerators, Spectrometers, Detectors and Associated Equipment), vol. 579, no. 1, 2007* pp. 363-366.

[4] T. Niedermayr *et al.*, "Gamma-ray imaging with a coaxial HPGe detector," *Nuclear Instruments and Methods in Physics Research, Section A (Accelerators, Spectrometers, Detectors and Associated Equipment)*, vol. 553, no. 3, pp. 501-511, 2005.

[5] S. Agostinelli *et al.*, "Geant 4 - A simulation toolkit," *Nuclear Instruments and Methods in Physics Research, Section A (Accelerators, Spectrometers, Detectors and Associated Equipment)*, vol. 506, no 3., pp. 250-303, 2003.

[6] R.M. Kippen, "The GEANT4 low energy Compton scattering (GLECS) package for use in simulating advanced Compton telescopes," *New Astron. Rev.*, vol. 48, no. 1-4, pp. 221-225, 2004.

[7] A. Lechner, M.G. Pia and M. Sudhakar, "Validation of Geant4 Low Energy Electromagnetic Processes Against Precision Measurements of Electron Energy Deposition," *IEEE Transactions on Nuclear Science*, vol. 56, no. 2, pp. 398-416, 2009.

[8] E. Wulf *et al.*, "Germanium Strip Detector Compton Telescope Using Three Dimensional Readout," *IEEE Transactions on Nuclear Science*, vol. 50, no. 4, pp. 1182-1189, August 2003.

[9] K. Vetter *et al.*, "Gamma-ray imaging with position-sensitive HPGe detectors," *Nuclear Instruments and Methods, Section A (Accelerators, Spectrometers, Detectors and Associated Equipment)*, vol. 525, pp. 322-327, 2004.

[10] K. Vetter *et al.*, "Large-Volume Si(Li) Orthagonal-Strip Detectors for Compton-Effect-Based Instruments," *IEEE Trans. Nucl. Sci.*, vol. 52, no. 6, pp. 3181-3185, December 2005.

[11] T. Tanaka *et al.*, "Development of a Si/CdTe semiconductor Compton telescope," *High-Energy Detectors in Astronomy, Proceedings of SPIE*, vol. 5501, pp. 229-268, 2004.

[12] J.P. Sullivan, *et al.*, "Detector tests for a prototype Compton imager," *IEEE Nuclear Science Symposium*, vol. 2, pp. 1384-1388, 2003.

[13] D. Xu *et al.*, "4π Compton imaging with single 3D position sensitive CdZnTe detector," *Hard X-Ray and Gamma Detector Physics VI, Proc. SPIE*, vol. 5540, pp. 144-155, 2004.

[14] E. Aprile *et al.*, "The LXeGRIT Compton Telescope Prototype: Current Status and Future Prospects," *Proc. SPIE*, vol. 4851, pp. 1196-1209, 2003.

[15] M.J. Berger *et al.*, "XCOM: Photon Cross Sections Database," *NIST Standard Reference Database 8 (XGAM)*, 2009.

[16] A. Einstein, "On a heuristic viewpoint concerning the production and transformation of light," *Annalen der Physik*, vol. 17, pp. 132-148, 1905.

[17] A. Compton, "A Quantum Theory of the Scattering of X-rays by Light Elements," *The Physical Review*, vol. 21, no. 5, pp. 484-501, 1923.

[18] P. Weilhammer *et al.*, "Si pad detectors," *Nuclear Instruments and Methods in Physics Research, Section A (Accelerators, Spectrometers, Detectors and Associated Equipment)*, vol. 383, pp. 89-97, 1996.

[19] C. Ordonez, A. Bolozdynya and W. Chang, "Doppler Broadening of Energy Spectra in Compton Cameras," *IEEE Nuclear Science Symposium*, vol. 2, pp. 1361-1365, 1997.

[20] O. Klein and Y. Nishina, "Scattering of radiation by free electrons on the new relativistic quantum dynamics of Dirac," *Zeitschrift fur Physik*, vol. 52, no. 11-12, pp. 853-868, 1929.

[21] Integrated Detector and Electronics AS (IDEAS), "VA32_Rich2 Specifications v0.90," *http://www.ideas.no/products/ASICs/pdf/Va32_Rich2_v0_90.pdf.*

[22] Integrated Detector and Electronics AS (IDEAS), "TA32CG2 Description," *http://www.ideas.no/products/ASICs/pdf/TA32cg2.pdf.*

[23] Saint Gobain Crystals, "CsI(Tl)," *http://www.detectors.saint-gobain.com.*

[24] Hamamatsu, "S3590-01 Silicon PIN Photodiode" *http://hamamatsu.com.*

[25] Hamamatsu, "H4083 Charge Amplifier" *http://hamamatsu.com.*

[26] Saint Gobain Crystals, "Brillance 380," *http://www.detectors.saint-gobain.com.*

[27] R. Brun *et al.*, "ROOT - An Object Oriented Data Analysis Framework", *CERN, Geneva, Switzerland*, http://root.cern.ch. 1995-2007.

[28] M. Matsumoto and T. Nishimura, "Mersenne Twistor: A 623-dimensionally equidistributed uniform pseudorandom number generator," *ACM Transactions on Modeling and Computer Simulation*, vol. 8, no. 1, pp. 3-30, 1998.

[29] The source was made by Isotope Products *www.ipl.isotopeproducts.com.*

[30] C. Lehner it et al., "4π Compton Imaging Using a 3-D Position Sensitive CdZnTe Detector Via Weighted List-Mode Maximum Likelihood," *IEEE Transactions on Nuclear Science*, vol. 51, no. 4, pp. 1618-1624, 2004.

[31] J.P. Sullivan, S.R. Tornga and M.W. Rawool-Sullivan, "Extended radiation source imaging with a prototype Compton imager," *Applied Radiation and Isotopes*, vol. 67, pp 617-624, 2009.

[32] M.W. Rawool-Sullivan *et al.*, "A simple algorithm for estimation of source-to-detector distance in Compton imaging," *Applied Radiation and Isotopes*, vol. 66, pp 1986-1991, 2008.

[33] A. Zoglauer, "First Light for the Next Generation of Compton and Pair Telescopes," *Doctoral Thesis, Munich University of Technology, Germany*,

[34] S.R. Tornga *et al.*, "Three-Dimensional Compton Imaging Using List-Mode Maximum Likelihood Expectation Maximization," *IEEE Transactions on Nuclear Science*, vol. 56, no. 3, pp. 1372-1376, June 2009

[35] M. Hynes *et al.*, "The Raytheon-SORDS trimodal imager," *Proc. Soc. Photo-Opt. Instrum. Eng. (SPIE)*, vol. 7310, 2009

[36] D. Wakeford *et al.*, "The SORDS trimodal imager detector arrays," *Proc. Soc. Photo-Opt. Instrum. Eng. (SPIE)*, vol. 7310, 2009

[37] R. Dicke, "Scatter-Hole Cameras for X-Rays and Gamma Rays," *Astrophys. J.*, vol. 153, iss. 2P2, pp. L101, 1968

[38] E. Fenimore, T. Cannon, "Coded Aperture Imaging with Uniformly Redundant Arrays," *Appl. Opt.*, vol. 17, no. 3, pp. 337-347, 1978

[39] A. Dempster, N. Laird and D. Rubin, "Maximum Likelihood from incomplete data via the EM algorithm," *J. Royal Statist. Soc.*, vol. B39, pp. 1-38, 1977.